August 2021

Study of Lead Sulfate Growth Kinetics in Lead Acid SLI Batteries

Dustin Wenninger
University of Wisconsin-Milwaukee

STUDY OF LEAD SULFATE GROWTH KINETICS IN LEAD ACID SLI SECONDARY BATTERIES

by

Dustin J. Wenninger

A Thesis Submitted in
Partial Fulfillment of the
Requirements for the Degree of

Master of Science
in Engineering

at

The University of Wisconsin-Milwaukee
August 2021

ABSTRACT

STUDY OF LEAD SULFATE GROWTH KINETICS IN LEAD ACID SLI BATTERIES

by

Dustin J. Wenninger

The University of Wisconsin-Milwaukee 2021
Under the Supervision of Dr. Ben Church

The importance of a safe and reliable way to both store and use energy, has led to a significant amount of research in the field of secondary battery development and refinement. The thesis herein explores a new application of a mature technology that has proven viable for internal combustion engines (ICE). Though the technology has proven viable for the start, lighting, and ignition, of conventional ICEs, the development of such advanced battery systems to meet the energy demands of Hybrid Electric Vehicles (HEV) is not without challenge. Lead acid SLI secondary batteries have demonstrated high recyclability, low self-discharge, good performance at both low and high temperatures, while also being cost effective. However, several of the main drawbacks to this technology include battery weight, limited cycle life, loss of capacity from sulfation, corrosion of the electrodes, and degradation of active material, among others, which precludes their widespread adoption over more expensive battery chemistries. The high currents involved with regenerative braking technologies, as well as operation under high rate partial state of charge (HRPSoC) conditions as a function of start-stop technologies, and the resultant cell degradation, has led to much research in the direction of performance advancements while maintaining the positive benefits and cost effectiveness. The complexity of the HRPSoC conditions induced during HEV operation has made development of mitigations strategies for observed cell degradation mechanisms both difficult and expensive. In particular, the sulfation that occurs at the negative plates is of high concern. Through the combination of cyclic voltammetry (CV) and scanning electron microscopy (SEM), a fundamental understanding of the lead sulfate growth kinetics could be studied more easily. In this work, several paste compositions for the negatively active material (NAM) were prepared to study the individual additive's effects on lead sulfate growth kinetics at the negative plate. Additionally, by modifying the number of cycles endured and coarsening duration, the resultant impacts of those variables on the lead sulfate growth kinetics were investigated. From the results, the greatest reduction in lead sulfate crystallization and growth, with corresponding NAM additives were predicted, with the samples containing carbon additives having the greatest impacts relative to the lead only control sample. Experimental challenges were observed, such as corrosion of the current collectors,

delamination of the working electrodes, and non-homogenous distribution of additives present, which may have contributed deviations from theoretical expectations. It is anticipated that the developed three-electrode test cell developed in conjunction with the aforementioned analytical techniques, can be readily applied to rapidly evaluate the efficacy of NAM additives in the retardation of lead sulfate crystallization and growth kinetics.

DEDICATIONS

The work herein is dedicated to all of those that have supported me both consciously and unconsciously throughout this long and arduous process. You know who you are, and I cannot thank you enough. You have truly helped to positively shape my future.

In loving memory of my grandparents
Bob & Rosie

TABLE OF CONTENTS

LIST OF FIGURES

LIST OF TABLES

LIST OF ABBREVIATIONS

SLI	Start Light Ignition
DCA	Dynamic Charge Acceptance
$PbSO_4$	Lead Sulfate
H^+/H_2	Hydrogen Ion/Hydrogen
NAM	Negatively Active Material
OCV	Open Circuit Voltage
dV/mV/V	delta voltage/millivolt/Volt
LAB	Lead Acid Battery
VRLAB	Valve Regulated Lead Acid Battery
AGM	Absorbent Glass Mat
HEV	Hybrid Electric Vehicle
PHEV	Plug-In Hybrid Electric Vehicle
CV	Cyclic Voltammetry
HRPSoC	High-Rate Partial State of Charge
µm	micron(s)
g/cm^3	grams per cubic centimeter
SoC	State of Charge
L	Liter
H_2SO_4	Sulfuric Acid
kg	kilogram
°C	Degrees Celsius
$mA\ cm^{-2}$	milliamp per square centimeter
PbO/PbO_2	Lead Oxide/Lead Dioxide
Ka	Acid Dissociation Constant
C	C-Rate
Hg	Mercury
$HgSO_4$	Mercury Sulfate
wt%	weight percent
Hz	Hertz
g	gram
PVDF	Polyvinylidene Fluoride
NMP	N-Methyl-2-Pyrrolidone
mm	millimeter
mils	thousandth of an inch
Pt	Platinum
g/L	grams per liter
g/mL	grams per milliliter
mV/s	millivolts per second
KX	1,000 X Magnification
Si	Silicon
DoD	Depth of Discharge

EDS	Energy Dispersive Spectrometry
K_2SO_4	Potassium Sulfate
Pb/Pb^{2+}	Lead/Lead Ion
SEM	Scanning Electron Microscope/Microscopy
XRD	X-Ray Diffraction

ACKNOWLEDGMENTS

I would first like to acknowledge Dr. Benjamin Church for his tireless efforts and inexhaustible patience in aiding me to complete this work. Dr. Church served as an inspiration ever since the topic was first introduced and provided all he could to see this work through to completion. I would also like to formally acknowledge both my family and friends for their never-ending enthusiasm, encouragement, and reassurance when I needed it most. A special thanks goes out to Mr. Shengyi Li, Mr. Bryce Erwin, Mr. Joshua Harris, Mr. Robert Hansen, and Mr. Marshall Schinner, as well. I could not have completed this work without you!

Thank You All.

Chapter 1 – Introduction

1.1 Overview

The introduction of new fuel efficiency standards, consumer driven increases in performance, improved safety, as well as the hybridization of mechanical and electrical drivetrains, will lead to an increase in demand for electrical power, and by extension impose new requirements for the electro-chemical storage device used in automobiles, the lead acid battery. Lead acid batteries retain a leading position within the automotive industry as the primary choice for start, light, ignition (SLI) applications, with an estimated annual world market of USD 38.2 billion in 2010 [1]; however, with advent of more demanding technologies, such as start-stop and regenerative braking, improvements in performance are required to withstand the repeated cycling of high-rate charges without sustaining long-term performance degradation. This performance metric is commonly referred to as dynamic charge acceptance (DCA) and is related to two main factors: the ability of the battery to withstand electrochemical overpotentials without electrolyzing the electrolyte, which results in the evolution of H_2 gas, and the kinetics of the lead sulfate ($PbSO_4$) reduction on the negatively active mass (NAM) [2]. The work herein provides a discussion concerning the development of a fundamental understanding of the kinetics of $PbSO_4$ reduction on the NAM, while also contributing to the future development of related research assessing how various other factors affect the kinetics of $PbSO_4$ reduction.

The initial chapter will give a general introduction of the topic, personal motivations, and will formally address the proposed objectives of the research that follows. This first portion includes a brief preface for the lead-acid secondary cell, which will be further elaborated on in the second chapter, while also providing a general introduction to hybrid electric vehicles, and cyclic voltammetry.

1.1.1 The Lead Acid Secondary Cell

The lead-acid cell is an electrochemical secondary battery that utilizes a liquid electrolyte and two solid electrodes. The electrodes are composed of a porous lead structure for the negative electrode, and lead oxide for the positive electrode. The negative and positive electrodes are both immersed in a sulfuric acid electrolyte solution and connected by an electrical conductor (Fig. 1.1). During discharge of the cell, lead sulfate is formed on both the negative and positive electrodes, by means of redox reactions. The reaction is fully reversible, and both electrodes revert to their original states during charging.

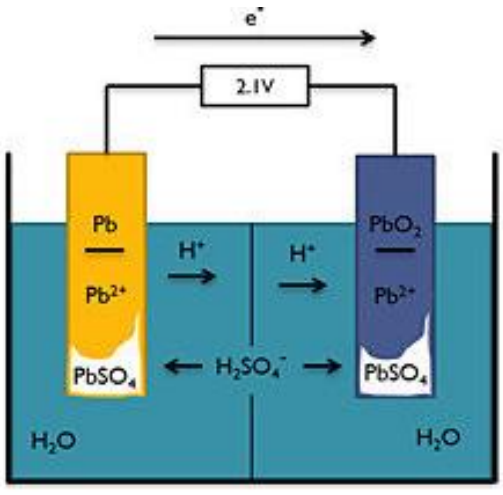

Fig. 1.1 – Lead Acid Secondary Cell Diagram [3]

The electrical potential differences between the negative and positive electrodes when not connected to an electrical load is known as its Open Circuit Voltage (OCV), which in the case of the aforementioned cell is roughly 2.1V. The individual cells are then stacked and connected to attain larger voltages. The next subsection will provide a brief history of the lead acid batteries, which begins by detailing the inventions of its predecessors, before culminating with the invention of the lead acid battery.

1.1.2 Lead Acid Historical Perspective

The lead acid battery can trace its humble beginnings to the invention of the voltaic pile by Alessandro Volta in 1800 (Fig. 1.2). Volta's design of the voltaic pile consisted of copper and zinc discs, which were separated by either brine-soaked cloth or cardboard (Fig. 1.2). Volta's batteries suffered from a relatively short lifetime due to polarization of the copper as well as accelerated degradation of the zinc due to short circuits caused by impurities within the material, in a phenomenon called local action. The premature zinc degradation was later mitigated in 1835 when William Sturgeon discovered that amalgamation of the zinc prevented local action [4].

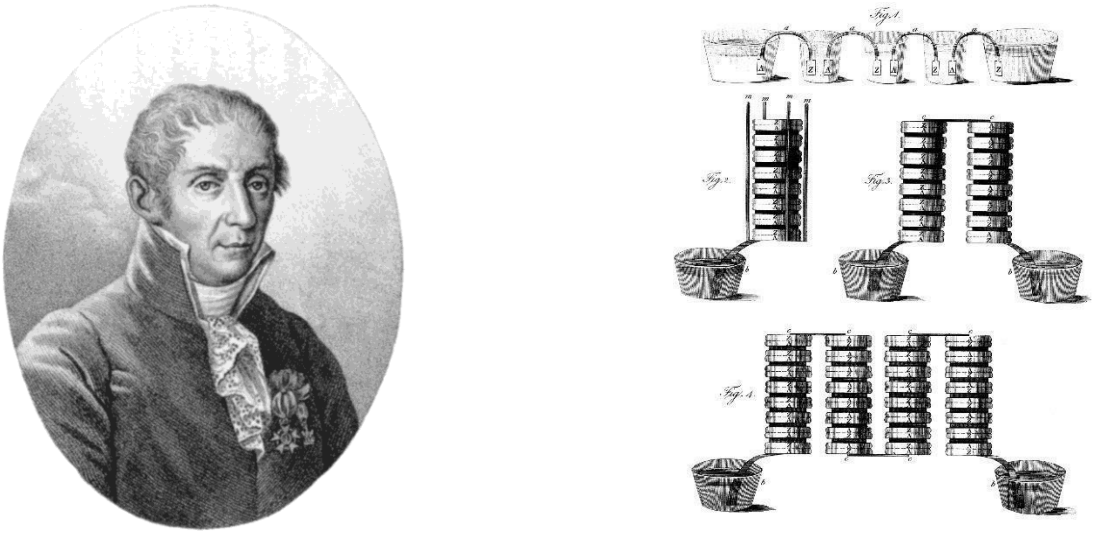

Fig. 1.2 – Portrait of Alessandro Volta (Left) [5], Volta's Original Illustration of Crown of Cups & Voltaic Pile Batteries Published in 1800 (Right)

The solution to the polarization problem that plagued the voltaic pile came just a year later when John Frederic Daniell (Fig. 1.3) invented the Daniell cell, which had a second electrolyte. The presence of this second electrolyte served to consume the hydrogen lost by the first electrolyte. The porous pot version of the Daniell cell, invented by John Dancer, an instrument maker in Liverpool, England, was composed of a copper pot filled with a copper sulfate solution. Immersed in this solution, was an unglazed non-vitreous pottery container filled with a sulfuric acid solution and a zinc electrode [6]. The incorporation of the non-vitreous pottery as the material for the inner container allowed for ion transfer of the two electrolytes to occur, but still allow for separation of the electrolytes, due to the inherent porous nature of non-vitreous pottery. This design (Fig. 1.3) offered the benefits of a safer and less corrosive operation, which by extension offered longer battery life relative to the

voltaic piles that came before. The Daniell cell was so well received that it went on to become the industry standard of batteries employed by the telegraph network, as well as became the historical basis for the definition of the unit of the electromotive force, the volt, where the Daniell cell had an emf of approximately one volt [7].

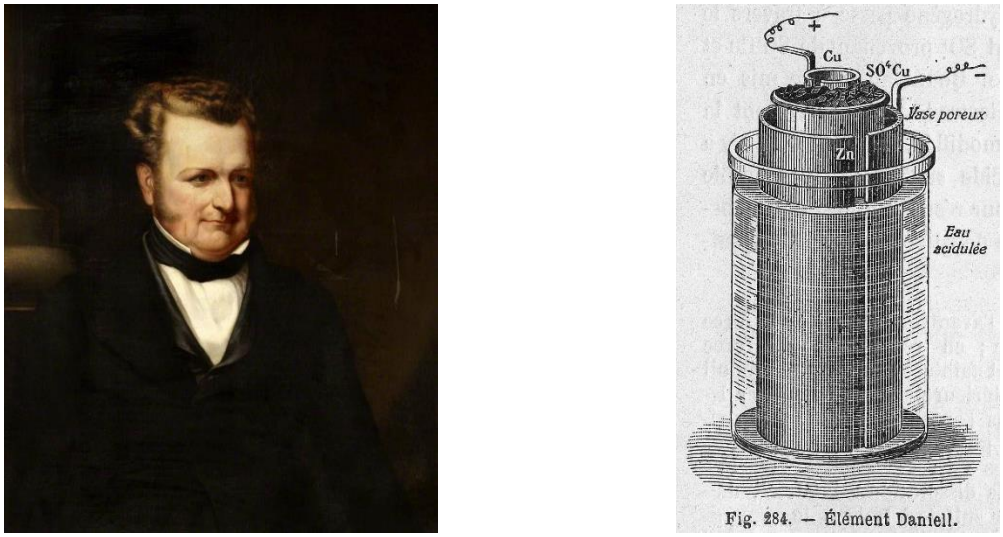

Fig. 1.3 – Portrait of John Frederic Daniell (Left), Daniell (Porous Pot) Cell (Right)

Various improvements were made to the Daniell cell over the years following its invention; however, up until this point, batteries were one-time use, commonly referred to as a primary cell. All that was about to change when the lead-acid secondary cell was discovered by French Physicist Gaston Plante (Fig. 1.4) in 1859. The unique feature of the battery that Plante invented was the battery's ability to be recharged by means of passing a reverse current through the system. Gaston Plante had been studying the polarization of two identical electrodes immersed in a solution of diluted sulfuric acid, when he discovered a phenomenon, he termed secondary current. He noticed that this secondary current was the

highest for the system containing lead plates with rubber separator sheets in a 10% sulfuric acid solution, as well as having the highest voltage too (Fig 1.4).[8]

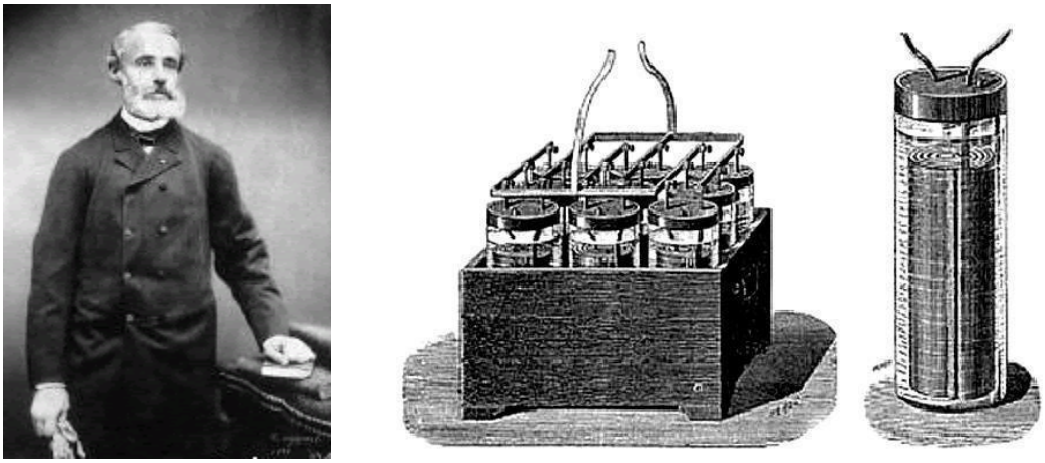

Fig. 1.4 – Portrait of Gaston Plante (Left), First Rechargeable Lead Acid Battery (Right) [8]

Following the invention of the first rechargeable battery, many notable advancements to Plante technology took place. In 1881 Camille Alphonse Faure, a French chemical engineer, made improvements to the plates to consist of a lead grid lattice, with a pressed lead oxide paste. This design improved the manufacturability of the battery. Other improvements include alloying of the lead grids in 1935, development of a gel electrolyte to oppose leakage with different cell designs in 1957, to the invention of valve-regulated lead acid batteries in the 1967 to combat water loss [8], as well as development of absorbed glass mat types, which allowed for the valve-regulated batteries to be maintenance free, leading to the culmination of the batteries we use today, which are produced in a variety of different types, and used in a multitude of different applications, which will be discussed in greater detail in the next subsection.

1.1.3 Types & Applications

Over the years Lead Acid Batteries (LAB) roles have become diversified from serving as an electrical source for vehicles to acting as backup power supplies for applications where a reliable power source is needed. LABs come in many variants and are classified by either their type/application or their maintenance requirements.

SLI batteries are the LABs people are most familiar with as they are used in automobiles (Fig. 1.5). They are responsible for providing the electrical energy necessary to start the vehicle, run the various accessories (headlights, radio, climate control, etc.), and lastly for ignition. They are designed to provide rapid bursts of energy, and as such have a greater number of plates than their deep cycle variants. The greater number of thinner plates present allows for a larger surface area of active material to participate in the electrochemical reaction and therefore deliver the maximum current output.

Fig. 1.5 – Representative Image of a SLI Battery [9]

Motive power (Traction/Propulsion) batteries (Fig. 1.6) are most commonly found in industrial transport vehicles. These range from fork-lifts to the airline ground support vehicles, and even automated guided vehicles, which are found in manufacturing environments moving components, parts, or products from one area to another. Additionally, these batteries can be found powering golf carts, electric scooters, and electric wheelchairs. Motive power batteries are deep cycle batteries that are designed to be regularly discharged of most of their capacity. The amount of discharge is usually between 45 to 75 % [8] of its total capacity depending on its application. Deep cycle batteries differ from SLI batteries, by having less of and thicker plates. Additionally, the plates also have a higher density of active material present on the plates, and thicker separators between them, all of which does not allow for as high of a peak current but does allow for greater longevity of the battery under deep discharge cycling operations.

Fig. 1.6 – Representative Image of Motive Power Batteries [10]

Stationary batteries serve as a backup power supply by storing electrical energy from the grid for use during an electrical outage (Fig. 1.7). They are commonly used as backups for telecommunication systems, electric utility centers, and computer systems that necessitate 100 % up time [1].

Fig. 1.7 – Representative Image of Stationary Batteries [11]

Additionally, LABs are commonly classified in terms of their maintenance requirements, which come in two variants, those that require maintenance, and those that are maintenance free.

Flooded batteries are referred to as such because this type of battery has its plates completely submerged in the electrolyte solution. Usually, the optimal electrolyte solution level rests above the plates, acting as a reservoir to account for water loss upon charging.

Valve Regulated LABs (VRLAB) are commonly referred to as maintenance free, although this is somewhat of a misnomer given that these batteries will still require cleaning and functional testing throughout their lifetimes. VRLABs come in three main variants, Sealed VR wet cell, Absorbent Glass Mat (AGM), and Gel. The sealed VR wet cells are similar to the flooded batteries but differ with respect to a lack of user access to the case. Manufacturers of sealed VR wet cell batteries ensure that a sufficient amount of electrolyte is present in order to sustain the chemical reactions throughout the life of the battery under normal usage conditions. AGM VRLABs differ from their wet cell counterparts by utilizing fiberglass glass mat separator sheets to hold the electrolyte in a suspended state rather than in free liquid form. Because the electrolyte is suspended in close proximity to the plates, discharge and recharge efficiency should be enhanced and outgassing should be minimized. Similar to the AGM batteries, Gel VRLABs utilize a suspended electrolyte; however, silica additives are added to the electrolyte to transform from a liquid into a gel. The gel form of the electrolyte allows for very deep cycle applications, such as medical mobility scooter batteries. The Gel VRLABs are the most sensitive of the VRLABs in terms of adverse reactions that arise from over-voltage charging.

Over the years, SLI LABs have served as a robust and reliable method for the high current demands of automotive applications. The advent of Hybrid Electric Vehicles and their fuel saving techniques will increase the electrical demands of the automotive battery. The different types of Hybrid Electric Vehicles which will be discussed in the next subsection.

1.2 Hybrid Electric Vehicles (HEV)

With the knowledge that fossil fuels are a finite resource, coupled with the byproducts of their consumption most likely contributing to climate change by enhancing the greenhouse effect, an alternative to combustion technology for transportation is a necessity. In order to have a smooth transition from combustion engines to the next technology, hybrid vehicles, which use a combination of current combustion technology with electric motors were developed. Hybrid Electric Vehicles (HEV) come in several variants, which all depend upon how much of a role the electric motor plays in the propulsion of the vehicle.

Full HEVs are hybrids which utilize an electric motor and battery combination to propel the vehicle during times when the internal combustion engine functions with low efficiency or when high power is needed, such as starting from a stop, traveling at low speeds, or passing cars. When the vehicle is operating with the electric motor, the battery is partially discharged. Recharging of the battery comes from a combination of the internal engine and regenerative braking technologies, which converts the waste heat generated during braking into electrical energy. The electrical system operates at over 200 V [8], which is the highest operating voltage amongst HEVs. This type of HEV offers the greatest reduction in fuel consumption, with savings of nearly 40% [8]. The 2020 Toyota Prius (Fig. 1.8) is an example of a current production Full HEV.

Fig. 1.8 – 2020 Toyota Prius – Full HEV [12]

Mild HEVs differ from Full HEVs in what driving conditions the electric motor is used, the operating voltage of the electrical system, and reduction in fuel consumption. With mild HEVs, the electric motor is the primary operator during start up and accelerating only. The operating voltage of the electrical system is lower with a range of 100 – 200 V [8] typically. The less sophisticated system offers fuel savings of roughly 15 – 20% [8], which is highly dependent on driving conditions. The new 2020 Honda Insight (Fig. 1.9) employs Mild HEV technology.

Fig. 1.9 – 2020 Honda Insight – Mild HEV [13]

Micro HEVs are hybrids that are less sophisticated than both Full and Mild HEVs. Micro HEVs employ start-stop technology to reduce fuel consumption in situations where the car would normally idle, which tends to add up to a significant amount of time if driving in an urban environment. Start-stop technology works by turning the engine off when the car comes to a stop, such as at a stop sign or traffic light controlled intersection. The battery then provides the electrical energy needed to run the accessories. With less sophistication, the resulting reduction in consumption is only reduced by roughly 8% [8]. An example of a current production Micro HEV is the 2020 BMW 1 Series (Fig. 1.10).

Fig. 1.10 – 2020 BMW 1 Series – Micro HEV [14]

Plug-in HEVs (PHEV) are similar to full electric vehicles, in that they use the main power supply in order to charge the battery via an electrical outlet or a charging station. PHEVs come in two basic configurations, series PHEVs and Parallel PHEVs. Series PHEVs, commonly referred to as extended range electric vehicles are hybrids which use an electric

motor to turn the wheels. When the battery needs recharging, the internal combustion engine generates the electricity. Parallel PHEVs differ in that both the electrical motor and internal combustion engine are mechanically linked to the wheels, and therefore both contribute to turning the wheels under most driving conditions. During low speeds, when combustion is less efficient, the parallel PHEVs operate using solely the electric motors. The 2020 Kia Optima (Fig. 1.11) is one of Kia's hybrid offerings which uses Plug-in HEV technology.

Fig. 1.11 – 2020 Kia Optima – Plug-in HEV [15]

1.3 Cyclic Voltammetry

1.3.1 Cyclic Voltammetry Background

Voltammetry is the most widely used technique for acquiring qualitative information about electrochemical reactions [16]. There are numerous forms of voltammetry, such as potential step, linear sweep, and cyclic voltammetry, amongst others, and each of them vary slightly in the way that voltages or series of voltages are applied to the electrode and the measuring of the resultant current. As it pertains to this research project the scope will be limited to discussing only the cyclic voltammetry variant.

In cyclic voltammetry (CV), the voltage is swept between a potential range at a fixed scan rate from V_1 to V_2. Upon reaching the potential at V_2, the scan is then reversed, and the voltage is swept back to V_1, as shown in Figure 1.12. During the initial sweep from V_1 to V_2 at reducing potentials lead sulfate begins to precipitate. Conversely, during the reverse sweep from V_2 to V_1 at oxidizing potentials the lead sulfate begins to dissociate.

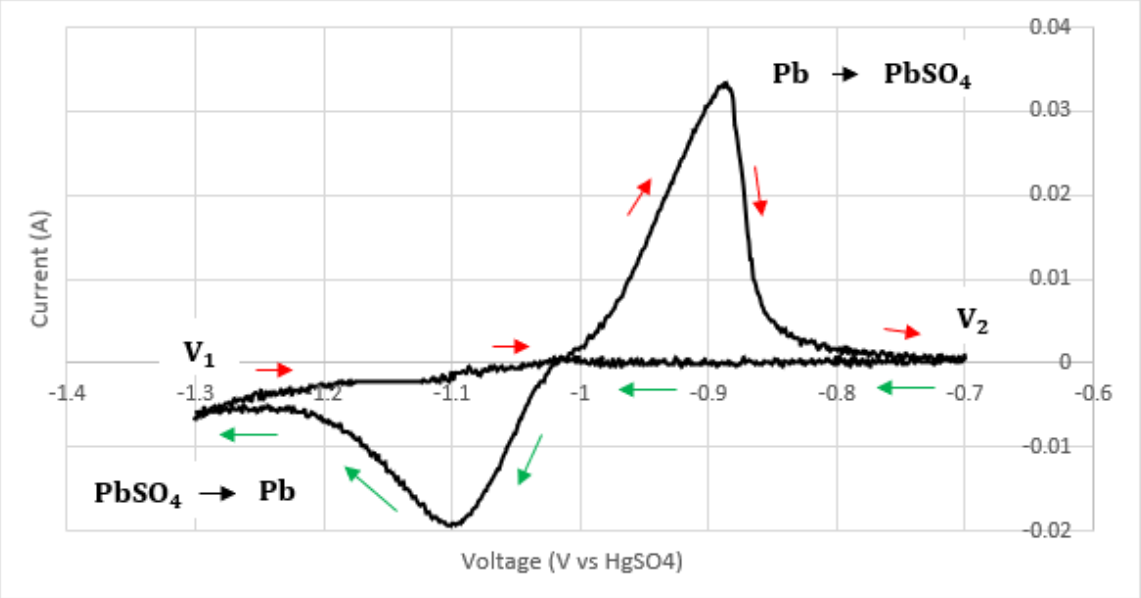

Fig. 1.12 – Representative Cyclic Voltammogram

1.3.2 Dynamic Charge Acceptance

The resultant cyclic voltammetry scan can be utilized to determine the dynamic charge acceptance (DCA) of the cell. DCA is a metric to characterize the rechargeability of the battery [17]. The ability to characterize the battery's ability to accept charge is important due to HEVs use of fuel saving technologies such as regenerative braking, which critically depend on the DCA of the battery [18]. Of particular importance is the Pb^{2+} ion dissolution at the negative electrode, which is the rate limiting step during micro-cycle charging [19]. Integration of the CV curve in the area where the $PbSO_4$ reverts to Pb allows us to calculate the DCA. The method of calculation will be discussed in greater detail in Chapter 3.

1.4 Motivations

The lead-acid battery has been first choice for SLI applications of the automobile industry, with an estimated 320 million units shipped in 1999 [20]. However, improvements in performance are necessary in order to meet the demanding applications of new cars being designed and produced. Regenerative braking and start-stop technologies will demand improved DCA performance, which is a metric for measuring the battery's ability to accept and supply a high-rate of charge repeatedly without suffering degradation of long-term performance. The shortcoming that lead-acid batteries face during the regenerative braking process, is degradation of the grid from the high levels of current involved during the storage of electrical energy from the reclaimed brake waste heat. The degradation of the battery from the start-stop technology is attributed to the formation of large lead sulfate crystals during the reduction on the negatively active material, which under the conditions of start-stop, will not dissolve back into solution.

The ability to utilize LAB cells in HEV applications would further diversify LABs applications in the automotive field by capitalizing on the mature technology; however, in order to do so, a quantitative understanding of the growth kinetics of lead sulfate will need to be developed. Previous work concerning a qualitative understanding of lead sulfate formation, and the retardation of their formation by use of various additives to the active material will be discussed in the following section.

1.4.1 Previous Work/Related Research

The use of VRLA batteries in SLI applications for HEV applications, with the cells operating under High-Rate Partial State of Charge (HRPSoC) conditions, leads to a build-up of $PbSO_4$ at the negative plates. This unique phenomenon was first studied by scientists at the Japan Storage Battery Company (JSB) in their development of VRLAs for HEV applications. Their research focused on the benefits of employing increased concentrations of carbon black into the NAMs, in which they showed that increasing the concentration of carbon black to the NAM, helped to resist accumulation of $PbSO_4$ on the plate [21].

In addition to carbon additives, other inhibitors of $PbSO_4$ recrystallization, such as poly-aspartic acid, have been shown to significantly retard the growth of $PbSO_4$ crystals by means of forming smaller $PbSO_4$ crystals, which are highly soluble and sustain a high concentration of Pb^{2+} ions in the solution, thereby increasing DCA. Additionally, the poly-aspartic acid was found to increase the overpotential of H_2 evolution [22].

The measurement of the kinetics of $PbSO_4$ reduction has not been conducted in a quantitative manner but is necessary to be able to statistically compare rates between systems with metallurgical differences in electrode chemistry, differences concerning the

additives present in the electrolyte, or other industry techniques utilized to minimize $PbSO_4$ growth.

1.5 Research Objectives

The proposed objectives of the current research aim to address several of the previously mentioned shortcomings of using LABs in HEV applications, mainly the rapid degradation of the negative plates due to sulfation. In particular, we will focus on the impacts of the various additives to the negatively active material (NAM) to lead sulfate growth kinetics. Specifically, the stated objective of this thesis is therefore:

- To develop a testing method that will allow for a fundamental understanding of the kinetics of $PbSO_4$ reduction on the negative electrode mass, when subjected to electrochemical overpotentials that minimize the formation of evolved gasses.

Though the main focus is developing a fundamental understanding of the growth kinetics of $PbSO_4$ reduction on the negative electrode mass, the testing method developed can also be used to evaluate the effects that additives have on DCA. Proposed design implementations and recommendations for improved testing will also be expressed in an effort to aid in the development of future test cells. The Chapters 2 and 3 will expand upon the introduced lead acid battery cell background, as well as to describe the experimental design. Chapter 4 will then present the results of the cyclic voltametric testing, including a thorough discussion of the effects of controlled variables on crystal growth and DCA. Lastly, Chapter 5 will summarize the work, and offer insights concerning future directions and limitations.

1.6 Hypothesis

Various compositions of the NAM, ranging from pure NAMs to NAMs containing multiple additives, will be subjected to cycling conditions where $PbSO_4$ formation is encouraged. It is theorized that the NAMs containing no additives will experience the greatest reduction in DCA, as a result of the formation of large, coarse $PbSO_4$ crystals. The NAMs containing additives should promote the formation of small readily dissolvable $PbSO_4$ crystals.

Chapter 1 References Cited

[1] Jung, Joey, et al. *Lead-Acid Battery Technologies: Fundamentals, Materials, and Applications*. CRC Press, Taylor & Francis Group, 2016.

[2] Kurzweil, P. "Gaston Planté and His Invention of the Lead–Acid Battery—The Genesis of the First Practical Rechargeable Battery." *Journal of Power Sources*, vol. 195, no. 14, 2010, pp. 4424–4434., doi:10.1016/j.jpowsour.2009.12.126.

[3] Huang, Pei-Hsing, et al. "A New Application of the UltraBattery to Hybrid Fuel Cell Vehicles." *International Journal of Energy Research*, vol. 40, no. 2, 2015, pp. 146–159., doi:10.1002/er.3426.

[4] Sturgeon, William. *Scientific Researches, Experimental and Theoretical, in Electricity, Magnetism, ... Galvanism, Electro-Magnetism, and Electro-Chemistr*. FORGOTTEN Books, 2016.

[5] Finger, Stanley, et al. "Alexander Von Humboldt: Galvanism, Animal Electricity, and Self-Experimentation Part 1: Formative Years, Naturphilosophie, and Galvanism." *Journal of the History of the Neurosciences*, vol. 22, no. 3, 2013, pp. 225–260., doi:10.1080/0964704x.2012.732727.

[6] Watt, Alexander, and Arnold Philip. The Electroplating and Electrorefining of Metals. Merchant Books, 2006.

[7] Hamer, Walter J. "Standard Cells: Their Construction, Maintenance, and Characteristics." *National Bureau of Standards Monograph #84 US National Bureau of Standards*, 1965, doi:10.6028/nbs.mono.84.

[8] Pavlov Dečko D. Lead-Acid Batteries: Science and Technology: a Handbook of Lead-Acid Battery Technology and Its Influence on the Product. Elsevier, 2017.

[9] "SLI34-7 BCI GROUP 34 Automotive SLI Battery." *www.batterysharks.com*, www.batterysharks.com/SLI34-7-BCI-GROUP-34-Automotive-SLI-Battery-p/sli34-7_sli34-7.htm.

[10] "Getting Motivated About Motive Power." *Madland Toyota-Lift Blog*, www.madlandtoyota.com/news/forklift-batteries-chargers-motive-power.

[11] Mitchell, Roma. "Global Stationary Lead-Acid Battery Market 2019: Growth By Latest Technology With New Trends- 2024." *Medium*, Medium, 7 Oct. 2019, medium.com/@romamitchell13/global-stationary-lead-acid-battery-market-2019-growth-by-latest-technology-with-new-trends-2024-c107daf7bbbe.

[12] Admin. "Fuel Efficiency of the 2020 Toyota Prius." *Apple Valley Toyota*, 19 Sept. 2019, www.applevalleytoyota.com/blog/fuel-efficiency-of-the-2020-toyota-prius/.

[13] "2020 Honda Insight Review." *Autotrader*, Autotrader, www.autotrader.com/car-reviews/2020-honda-insight-review-281474979950585.

[14] Padeanu, Adrian. "2020 BMW 1 Series Officially Revealed With M135i Hot Hatch." *Motor1.Com*, Motor1.Com, 30 May 2019, www.motor1.com/news/351527/2020-bmw-1-series-revealed/.

[15] "2020 Kia Optima PHEV Plug-In Hybrid - Sedan Pricing & Features." *Kia*, www.kia.com/us/en/optima-plug-in-hybrid.

[16] Bard, Allen J., and Larry R. Faulkner. *Electrochemical Methods: Fundamentals and Applications*. John Wiley & Sons, 2004.

[17] E. Karden, P. Shinn, P. Bostock, J. Cunningham, E. Schoultz, D. Kok, J. Power

Sources 144 (2005) 505–512.

[18] Huang, Pei-Hsing, et al. "A New Application of the UltraBattery to Hybrid Fuel Cell Vehicles." *International Journal of Energy Research*, vol. 40, no. 2, 2015, pp. 146–159., doi:10.1002/er.3426.

[19] Budde-Meiwes, Heide, et al. "Dynamic Charge Acceptance of Lead–Acid Batteries: Comparison of Methods for Conditioning and Testing." *Journal of Power Sources*, vol. 207, 2012, pp. 30–36., doi:10.1016/j.jpowsour.2011.12.045.

[20] Linden, David, and Thomas B. Reddy. *Handbook of Batteries*. McGraw-Hill, 2002.

[21] Moseley, P.t., et al. "The Role of Carbon in Valve-Regulated Lead–Acid Battery Technology." *Journal of Power Sources*, vol. 157, no. 1, 2006, pp. 3–10., doi:10.1016/j.jpowsour.2006.02.031.

[22] Pavlov, D., and P. Nikolov. "Lead–Carbon Electrode with Inhibitor of Sulfation for Lead-Acid Batteries Operating in the HRPSoC Duty." *Journal of The Electrochemical Society*, vol. 159, no. 8, 2012, doi:10.1149/2.035208jes.

Chapter 2 – Lead Acid Cell Background

The lead acid cell is highly regarded for its high specific power, low self-discharge, ease of manufacture, and the incorporation of ubiquitous low-cost raw materials. This chapter aims to establish the general cell operation, construction of the cell via an introduction to the most important components, as well as to discuss cell degradation with regards to the anode. The initial section discusses the components of the cell and continues by detailing the manufacturing process, which is followed by an explanation of the electrochemistry that occurs during general operation of the cell before finally touching upon the cell degradation method of sulfation, where the growth kinetics of the lead sulfate crystals is of critical importance, in which this research seeks to understand.

2.1 Components of the Cell

The components of the LAB are similar to other secondary batteries of different electro-chemistries. They contain both positive and negative electrodes immersed in an electrolyte, which are isolated from one another via a separator material that facilitates ion transfer. They also all contain current collectors, which serve as an electrically conductive path to shuttle electrons from one terminal to the other. The components present within a typical valve-regulated lead acid battery are shown in Figure 2.1. Additionally, there are supplemental components that join several similar polarity electrodes together, as well as the container to contain the components; however, for the sake of brevity, only the grid, plates, separator sheets, and electrolytes will be further elaborated upon in the following subsections.

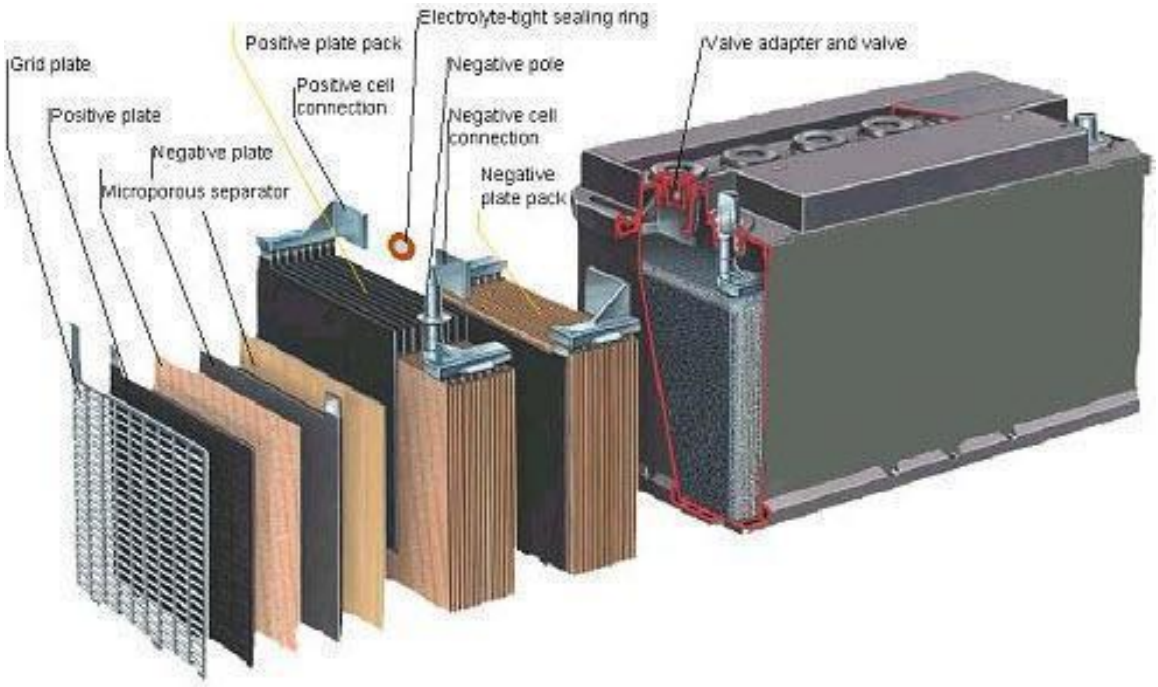

Fig. 2.1 – Cut-away of Valve-Regulated Lead Acid Battery Construction [26]

2.1.1 Grid – Current Collector

The grids of the battery serve two main functions. The first function is that they serve as the skeleton upon which to hold the active material. The second function is that they served as a current collector, which allows current to flow to and from all different areas of the plates. Lead-calcium-tin alloys are used for the production of plates for VRLABs, with slight changes in chemistry for the positive and negative plates. The presence of calcium within the alloy increases the mechanical properties of the alloy by precipitation strengthening. The increase in strength comes at the cost of increased corrosion susceptibility, which is countered by the addition of tin to the alloy. The main lead alloys used in the production of grids for different applications are shown in Figure 2.2.

Alloying Additives	Application
Antimony alloys 4—11 wt% Sb, As, Sn, Cu (Ag)	Flat plates, tubular plates for traction batteries, older types of stationary batteries
Low-antimony alloys 0.5—3.0 wt% Sb, Se, Cu, S, As, Sn (Ag)	Flat plates, tubular plates for low-maintenance or maintenance-free batteries: SLI, traction, stationary
Lead—calcium alloys 0.05—0.07 wt% Ca, 0—3% Sn (Al), Ag, Bi	VRLA batteries
Pure lead Sn	Planté plates, Bell Syst. Batt. punched grids (Gates)
Antimony—cadmium alloy 1.5 wt% Sb, 1.5 wt% Cd	GNB 'Absolyte battery'

Fig. 2.2 – Typical Lead Alloys Used During Grid Manufacturing [35]

2.1.2 Plates – Positive & Negative

The plates for both the positive and negative plate consist of pastes of active material on the aforementioned grid skeleton. The exact composition of pastes will have slight variances in compositions from manufacturer to manufacturer, and often have additives present that contribute to variances in performance. As such, these exact recipes are most likely regarded as a trade secret; however, conventional recipes are shown in Figure 2.3. The pasted plates are subjected to a curing process, which interlocked the particles into porous masses. The curing process is followed by a formation process, which electrochemically converts the porous masses into either positively active material or negatively active material.

Positive Active Material Recipe

Material	Unit	Amount
PbO	kg	25
H_2SO_4	L	1.6
Water	L	4.41
Pb_3O_4	kg	1.25
Graphite powder	kg	0.075
Paste density	g/cm³	3.7

Negative Active Material Recipe

Material	Unit	Amount
PbO	kg	25
H_2SO_4	L	1.5
Water	L	3.65
Barium sulfate ($BaSO_4$)	kg	0.2
Carbon black	kg	0.075
Sodium lignosulfonate	kg	0.04
Humic acid	kg	0.15
Paste density	g/cm³	4

Fig. 2.3 – Conventional positive active material (Left), and negative active material (Right) recipes [25]

2.1.3 Separator Sheets

Separator sheets are, as the name implies, used to separate the positive and negative plates from one another. They are typically composed of microporous polyethylene sheets or envelopes, with pore sizes between 5 – 30 μm [25]. The presence of the pores allows for ionic species present within the electrolyte access to the active material present on the plates. The polymeric portion of the separator sheets prevents short circuiting of the battery. AGMs are another commonly used type of separator sheets, which are formed from non-woven fabric composed of glass microfibers. Due to its highly porous nature, the AGM can absorb more acid than its polyethylene counterparts.

2.1.4 Electrolyte

The electrolyte is a dilute sulfuric acid solution, which conventionally contain additional additives, that increase the electrochemical activity by increasing the rate of $PbSO_4$ dissolution. In modern batteries it has been established that H_2SO_4 concentration should not exceed 1.28 g/cm^3, since this concentration provides the best cycling performance. During use however, the specific gravity of the electrolyte changes in relation to the state of charge (SoC) and can vary from 1.1 – 1.15 g/cm^3 during full discharge to 1.28 – 1.30 g/cm^3 during full charge [25].

2.2 Manufacturing of LABs

The manufacturing process for LABs is an eight-step process that starts with the production of lead oxide powder for use in pastes for both the positively and negatively active materials, and production of the grid and other cast components. The lead oxide is mixed with various additives and formed into pastes, which are then applied to the grids, and subsequently cured. Following the curing process, the plates are assembled into groups and placed into their respective battery containers. Electrolyte solution is added to batteries, which then soak for a period of time before current is applied in order to transform the paste into electrochemically active material. Following the formation process, the batteries are electrically tested and sealed, prior to labeling, palletizing, and shipping. An overview of the battery manufacturing process is shown in Figure 2.4.

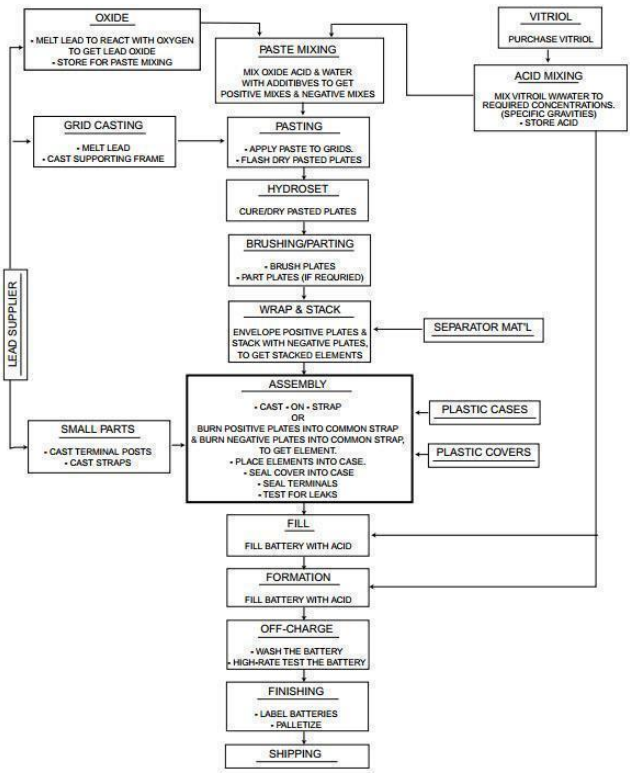

Fig. 2.4 – Flow Chart of the Battery Assembly Process [25]

2.2.1 Oxide & Grid Production Process

The lead oxide used to create the positive active material paste is produced either by means of the ball mill process or the Barton-pot process or purchased directly from an oxide producer. In the ball mill process, lead ingots are fed into a rotating mill where frictional heat generated by the tumbling oxidizes the surface of the ingot. The tumbling action also serves to remove the oxide layer, which reveals the underlying clean lead surface, allowing the cycle to repeat. The generated lead oxide powder is then carried via an airstream to a bag filter where it is collected. The Barton-pot process involves melting the lead ingots and feeding them into a reaction pot. The molten lead is rapidly stirred and atomized by a high-speed rotating paddle located at the bottom of the pot. The atomized molten lead is then reacted with oxygen to form lead oxide [25]. Representative images of a ball mill and Barton-pot used for the production of lead oxide, are shown in Figure 2.5.

Fig. 2.5 – Representative Images of the Ball Mill (Left) [27] & Barton-Pot (Right) [28] Processes

The grids are generally produced by either a casting or stamping operation (Figure 2.6). In the casting method, lead ingots are melted, and this molten lead is cast into dies which have the patterns of the battery grids. Once cooled, the raw castings are trimmed to

remove rough edges and gates. Battery grids made with the stamping process, involve stamping out battery grid patterns out of lead sheets (Figure 2.6).

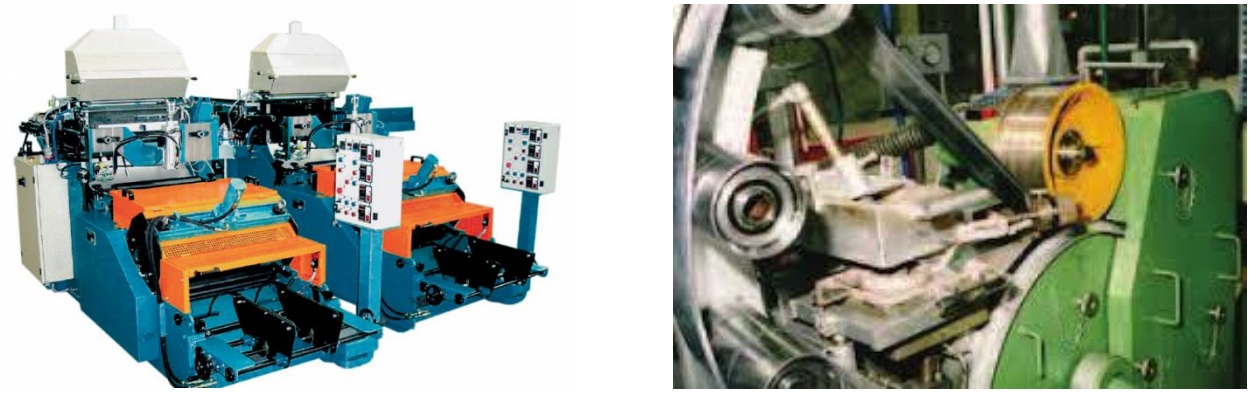

Fig. 2.6 – Representative Images of the Grid Casting (Left) [29] & Grid Stamping (Right) Processes

2.2.2 Pasting & Curing Process

Using the Faure process, the paste is mechanically applied to the spaces present within the grid, which is contrary to the Plante process where the active material is electrolytically developed out of the lead plates itself. Figure 2.7 shows a representative automatic battery grid pasting machine used for lead acid batteries.

Fig. 2.7 – Representative Image of the Grid Pasting Process [30]

Following the pasting process, the plates are then cured in ovens at a temperature of roughly 32 degrees centigrade for approximately 48 hours with a relative humidity of roughly 90 percent, as shown in Figure 2.8. After the curing process is complete the plates are then allowed to dry at ambient temperatures.

Fig. 2.8 – Representative Image of the Curing Process [31]

2.2.3 Assembly Process

The battery assembly process combines the cured plates, container, and other parts and transforms them from components into a functional battery. The assembly process consists of stacking the cured plates either by hand or aided by a machine that alternates positive and negative plates, which are separated by insulating separator sheets. In the SLI batteries that use AGM separator sheets, the plate groups require compression to a specific pressure, which is maintained by polymer tape. The similar polarity plates are then soldered into plate groups which are connected to the posts by a strap. The plate groups are then placed into containers and filled with electrolyte solution. The assembly processes are carried out with the use of an automatic stacking machine, automatic group insertion machine, and automatic acid filling machine, shown in Figure 2.9. The assembled batteries

then undergo a soaking and subsequent electrical formation process to become functional electrodes, which will be elaborated upon further in the next section.

(a) (b)

(c)

Fig. 2.9 – Representative images of automatic stacking machine (a), automatic group insertion machine (b), & automatic acid filling machine (c) [32]

2.2.4 Soaking & Formation Process

Once assembled the batteries are filled with a H_2SO_4 acid solution with a specific gravity of roughly 1.06, with amounts varying from 2.5 – 3.0 L per kg of cured paste. The plates are then left to soak in this solution for approximately 1 – 2 hours, after which time electric current is applied to begin the formation process, as shown in Figure 2.10.

During the formation process both the temperature and current are monitored and controlled. The temperature is kept between 25 and 50°C throughout the duration of the formation process. The formation current varies from 0.7 – 2.5 mA cm^{-2} throughout different stages in the formation process [35]. The duration of the formation process varies depending on the application, but typically lasts 18 – 30 hours for SLI batteries. The PbO present on the positive plates are converted to PbO_2 and $PbSO_4$ after the formation process. The PbO present on the negative plates is reduced to a spongy lead structure.

Fig. 2.10 – Representative Image of the Formation Process [25]

2.2.5 Testing & Sealing

Following testing of the battery for any short circuits, the battery cover will be sealed to the battery case, by either heat sealing, epoxy cement sealing, tar sealing, or epoxy glue sealing, as shown in Figure 2.11 [25].

Fig. 2.11 – Representative Image of the Testing & Sealing Process [33]

Assuming the batteries pass the electrical testing, they are subsequently labeled, palletized, and shipped.

2.3 General Cell Operation

Prior to the discussion concerning the half-cell reactions that occur, it should be noted that the sulfuric acid electrolyte is a strong acid. A strong acid is one that ionizes completely by losing one proton. Therefore, the first reaction that occurs prior to charging or discharging of the battery is the dissociation of the electrolyte in the manner shown in equation 1. This reaction occurs independently of the plates of the battery and is not an electrochemical reaction. Additionally, even though sulfuric acid is a diprotic acid, complete dissociation of the second proton will not occur for the most part, due to a low Ka2 value of roughly 0.012 [35].

$$\mathbf{H_2SO_4 \longrightarrow H^+ + HSO_4^-} \qquad \textbf{(EQ. 1)}$$

Upon discharge there is an electric field present in the electrolyte that drives the negative ions, bisulfate, towards the negative plate. At the surface of the negative plate, the bisulfate reacts with the porous lead structure and is oxidized to form lead sulfate, as shown via equation 2. This reaction also produces positive ions, H+, which are repelled by the aforementioned field, and two electrons, which are delivered to the terminal, and subsequently used to conduct work.

$$\textbf{At Negative Plate:} \quad \mathbf{Pb + HSO_4^- \longrightarrow PbSO_4 + H^+ + 2e^-} \qquad \textbf{(EQ.2)}$$

Simultaneously, the other half of the discharge reaction takes place at the positive plate. Three positive ions, H+, bisulfate, and the two electrons generated at the negative plate react with the porous leady oxide terminal and reduces to lead sulfate and two molecules of water, as shown via equation 3.

$$\textbf{At Positive Plate:} \quad \mathbf{PbO_2 + 3H^+ + HSO_4^- + 2e^- \longrightarrow PbSO_4 + 2H_2O} \qquad \textbf{(EQ. 3)}$$

When the two half-cell reactions are combined, we have both the negative and positive plate forming lead sulfate at the boundary between the electrodes and the electrolyte, as well as water, as shown via equation 4. All of the lead compounds that participate in the electrochemical reactions are insoluble and remain attached to their respective plates. The other products that participate in the reaction, sulfuric acid and water, are completely soluble, which is an important aspect that allows for the cell to be rechargeable. The other important aspect is that the chemical reactions that occur are reversible. In contrast, primary batteries typically have non-reversible reactions, and as such have reaction products that when formed are unavailable to participate in further reactions, such as the formation of either a gas or an insoluble precipitate.

Cell Reaction: $\mathbf{PbO_2 + Pb + 2H_2SO_4 \longrightarrow 2PbSO_4 + 2\,H_2O}$ **(EQ.4)**

The nominal voltage of the cell is roughly 2 V. These cells are connected in series to form either 6 V batteries or 12 V batteries depending on application. An overview of the chemical reactions is shown in Figure 2.12.

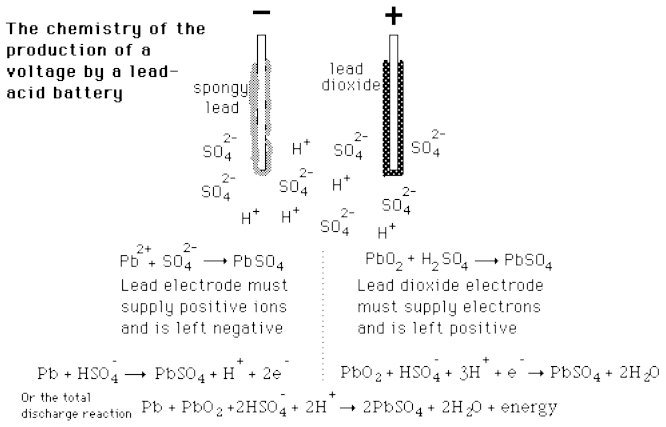

Fig. 2.12 – Schematic of the electrochemical reactions that take place during operation of lead-acid batteries [34]

2.4 Cell Degradation Mechanism

With the desire to use lead acid batteries in HEV applications, a better understanding of the cell degradation mechanisms will need to be ascertained. Operation under HRPSoC conditions and high current charging degrade a multitude of components within the battery in a variety of ways. Therefore, for the sake of brevity, the focus will consist of the degradation that occurs at the negative plate, and the scope will be restricted to the sulfation mechanism.

2.4.1 Sulfation

During regular operation of the battery, under a low rate of discharge (<0.4C), it is desirable for the formation of small $PbSO_4$ crystals during the discharge process, which will readily dissolve during the charging process. The rapid dissolution of the $PbSO_4$ crystals allows the active materials to revert to their original form, lead for the negative plate, or lead oxide for the positive plate. However, when subjecting the battery to HEV cycling conditions, a high rate of discharge (>0.4C) the $PbSO_4$ crystals are unable to fully dissolve into active material, and as a result coarsen. Over time the growth of this nonconductive $PbSO_4$ layer, leads to the formation of a passive film, which translates to a loss in battery capacity. During sulfation, the sulfuric acid electrolyte can become depleted of the sulfate ions, which results in several problems. A lack of sufficient sulfate ions, which act as charge conductors, will cause cell impedance to appear high and little charge current to flow.

During the discharge process at the negative plate, the half-cell reaction described in Equation 2, proceeds via two processes, shown in Figure 2.13. First, the porous lead of the negative plate reacts with HSO_4^- from the sulfuric acid to form Pb^{2+}, SO_4^{2-}, and H^+, in a

reaction called the "dissolution process". This reaction is an electrochemical process due to electron transfer. The electron transfer takes place only on electrically conductive sites, which in the case of the negative plate, is the metallic lead. Therefore, the rate of the electrochemical reaction is not only dependent upon diffusion of the HSO_4^- species, but also the effective surface area of the metallic lead. The porous structure of the metallic lead at the negative plate, allows for a significantly larger effective surface area compared to a solid chunk of lead.

- **Discharge process**

$$Pb + HSO_4^- \longrightarrow Pb^{2+} + SO_4^{2-} + H^+ + 2e^-$$

$$Pb^{2+} + SO_4^{2-} \rightleftharpoons PbSO_4$$

Fig. 2.13 – Discharge reactions at negative plate [37]

Following this reaction, the Pb^{2+} and SO_4^{2-} combine to form $PbSO_4$, in a chemical reaction referred to as either deposition or precipitation. The reaction rate is acid dependent; however, the solubility of $PbSO_4$ does not progressively track with increased sulfuric acid concentration, as evident in Figure 2.14. The solubility curve shows a maximum solubility of roughly 10 wt% sulfuric acid, which subsequently decreases rapidly at higher concentrations. The deposition of Pb^{2+} ions to $PbSO_4$ will progress at the fastest rate in locations that exhibit the highest concentration of acid.

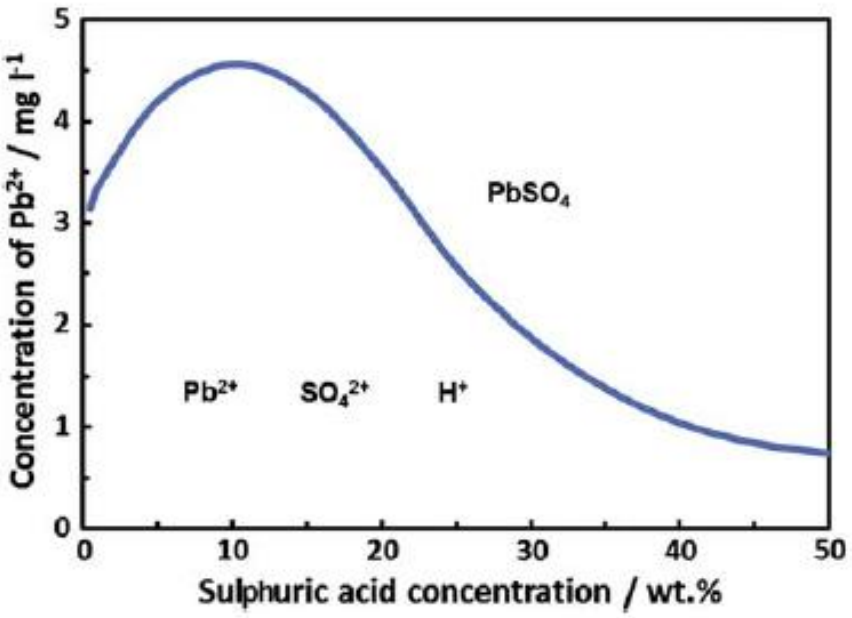

Fig. 2.14 – Solubility Curve of $PbSO_4$ in H_2SO_4 Solution [37]

The reaction rates of the dissolution and deposition processes will vary with respect to the rate of discharge. During discharge at a low rate, the dissolution of Pb to Pb^{2+} proceeds slowly. The associated consumption of HSO_4^- at the interior of the plate will also progress slowly, allowing for sufficient diffusion of the HSO_4^- from the bulk of the electrolyte. Consequently, the subsequent deposition rate of the Pb^{2+} to $PbSO_4$ will also occur slowly. The slow reaction rate of the deposition process is due to the low supersaturation of the Pb^{2+} in the sulfuric acid solution near the $PbSO_4$ crystal nucleation sites. As a function of the slow deposition rate, the newly formed $PbSO_4$ precipitates will preferentially form on the already deposited $PbSO_4$ crystals. The growth rate exceeds the nucleation rate, which results in desirable growth of variously sized and discontinuous $PbSO_4$ crystals on the surface, as well as the interior of the plate, as shown in Figure 2.15(a).

During discharge at a high rate, the lead sulfate formation proceeds in a different manner. The dissolution of Pb to Pb^{2+} proceeds so rapidly that the diffusion rate of HSO_4^-, cannot keep pace with consumption, and therefore tends to precipitate predominantly on the surface of the plate. Unlike the low-rate discharge, there is a high supersaturation of Pb^{2+} in the sulfuric acid solution near the $PbSO_4$ crystal nucleation sites. Consequently, the lead sulfate precipitates quickly on any available surface. Here the nucleation rate exceeds the growth rate, which results in the formation of a compact layer of small crystals at the surface of the plate. Eventually, this leads to a reduction in the effective surface area for electron transport, as well as prevention of HSO_4^- diffusion to the interior of the plate, as evident in Figure 2.15(b).

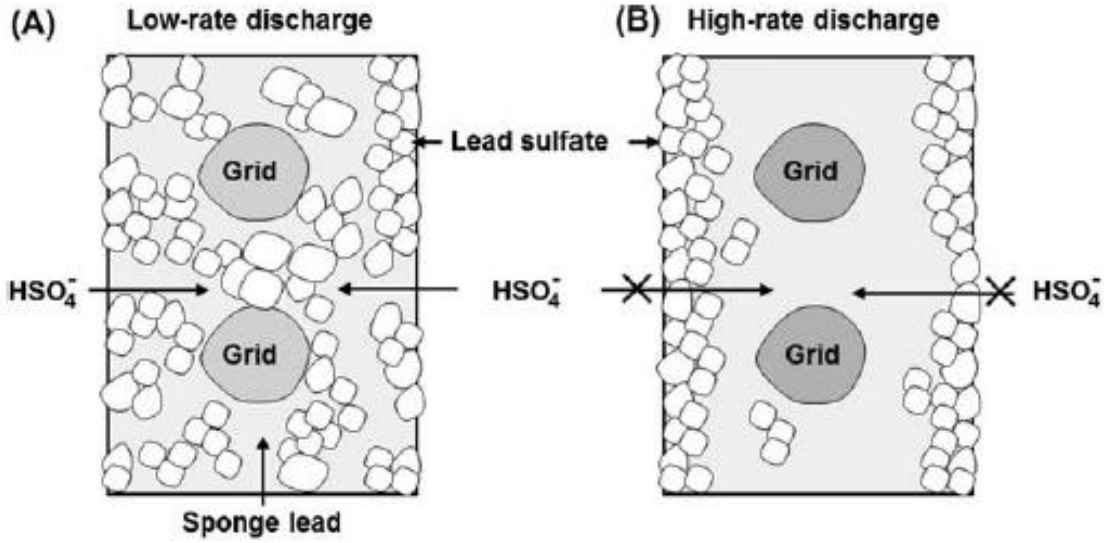

Fig. 2.15 – Schematic of lead sulfate distribution in a negative plate subjected to: (A) low-rate discharge (<0.4C) or (B) high-rate discharge (>0.4C) [37]

Similar to the discharging process, the charging process also proceeds via two similarly named reactions, dissolution and deposition. During the charging process however, the dissolution process is now the chemical reaction, while the deposition process is an electrochemical reaction. The reactions proceed in the manner shown in Figure 2.16, with the lead sulfate first dissociating into Pb^{2+} and SO_4^{2-} ions. At the same time, the SO_4^{2-} combines with H^+ ions from the sulfuric acid solution to form HSO_4^-. The electrons will preferentially flow to active sites in the NAM via the support grid, which has significantly less electrical resistance, relative to the discharged material, in order to reduce the Pb^{2+} to metallic lead.

- **Charge process**

$$PbSO_4 \rightleftharpoons Pb^{2+} + SO_4^{2-}$$

$$Pb^{2+} + SO_4^{2-} + H^+ + 2e^- \longrightarrow Pb + HSO_4^-$$

Fig. 2.16 – Charge reactions at negative plate [37]

During the reduction of the Pb^{2+} to metallic lead, hydrogen evolution, a competing reaction, occurs. The evolution of hydrogen normally only occurs near the end of the charging process due to a majority of the $PbSO_4$ having already been converted to metallic lead, causing a corresponding increase in the H^+ concentration. This increase in the H^+ concentration also slows further dissolution of $PbSO_4$.

Now, having thoroughly explained both the chemical and electrochemical reactions that occur both in the discharge and charging process, it is time to discuss the charging of the negative plate after having been deeply discharged at a low rate. As shown in Figure 2.15(a), the $PbSO_4$ has formed throughout the entire cross-sectional area of the plate. Additionally, due to the high utilization of the negatively active material, the specific gravity of the sulfuric acid solution is low. The reaction rate of the dissolution of $PbSO_4$ increases at low acid concentrations, as shown in Figure 2.14. The subsequent reduction of the Pb^{2+} ions to metallic lead proceed smoothly, minimizing the evolution of hydrogen. Utilizing an overcharge factor of roughly 10%, the plate can be returned to its fully charged state without issue. The same is true for plates that have undergone low rate PSoC cycling parameters with matching charging inputs and outputs. The overall SoC of the negative plate will degrade with cycling but can be normalized with the application of an equalization charge.

In stark contrast to the ease of charging exhibited by the negative plates deeply discharged at a low rate, the charging of plates deeply discharged at a high rate, is difficult. As shown in 2.15(b), the $PbSO_4$ does not form throughout the cross-sectional area of the plate, and instead stops at the surface of the plate, resulting in a low utilization of the active material, and consequently high acid concentration. The reaction rate of the dissolution of $PbSO_4$ decreases at high acid concentrations, as shown in Figure 2.14. The resultant lower concentration of Pb^{2+} ions, subsequently hinders the reduction of the ions to metallic lead. The electrons want to preferentially flow via the support grid, which has significantly less electrical resistance, relative to the discharged material; however, these electrons will

reduce some of the H+ ions prior to reaching the lead sulfate layer at the surface of the plate, as shown via Figure 2.17.

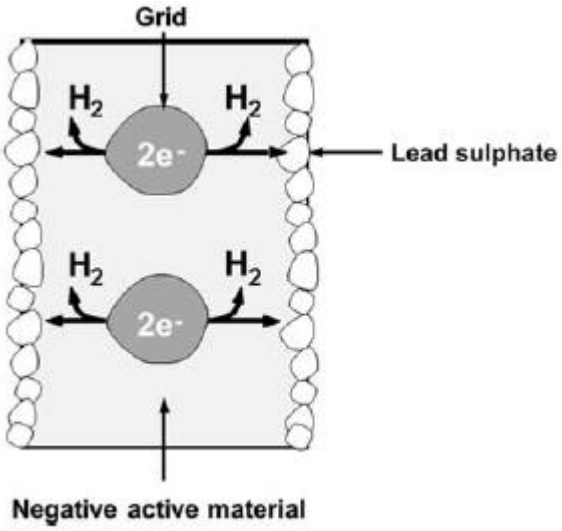

Fig. 2.17 – Schematic of the charging process of the negative plate post high-rate discharge [37]

Under HRPSoC conditions, some of the Pb^{2+} ions involved in the charge-discharge process, will contribute to the growth of larger $PbSO_4$ crystals through a recrystallization process shown in Figure 2.18. The resultant large $PbSO_4$ crystals, have a lower solubility relative to the smaller $PbSO_4$ crystals, and as a result coarsen overtime, which given enough cycling leads to progressive sulfation of the plate.

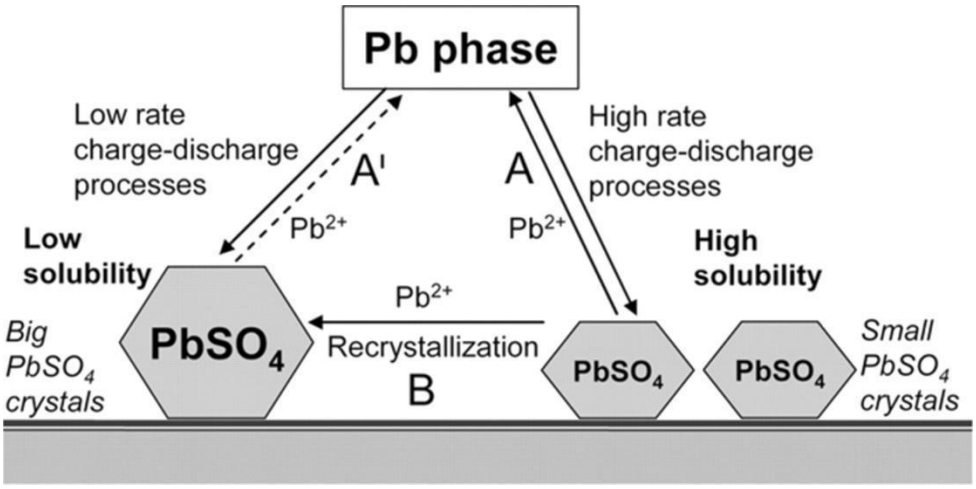

Fig. 2.18 – Schematic of the basic processes that take place at the negative plates of lead-acid batteries cycled under HEV operating conditions [36]

Even with the utilization of an overcharge factor of roughly 10%, complete conversion of the $PbSO_4$ at the surface of the plate cannot be realized. The issue is further compounded with VRLA batteries, where the charging process will also be inhibited by the oxygen recombination reaction. Additionally, the overcharge factor is dynamic, and increases with continued cycling, due to progressive water loss. This water loss causes the separator sheets to dry out, increasing the amount of oxygen reaching the plates, which exacerbates the oxygen recombination occurring.

Chapter 2 References Cited

[23] https://www.osha.gov/SLTC/etools/battery_manufacturing/glossary.html#Ball Mill Process

[24] https://prod.sandia.gov/techlib-noauth/access-control.cgi/2004/043149.pdf

[25] Jung, J., Zhang L., Zhang J. "Lead-Acid Battery Technologies: Fundamentals, Materials, and Applications"

[26] Sidi, Purnomo, et al. "Electric Energy Management and Engineering in Solar Cell System." Solar Cells - Research and Application Perspectives, June 2013, doi:10.5772/52572.

[27] "Lead Oxide Ball Mill." Lead Oxide Ball Mill | Fully Automatic PLC Control Plant, https://acsengineering.in/ball-mill-oxide-system.php.

[28] "Barton Reactors." Eagle Oxide Services, https://www.eagleoxide.com/product/barton-reactors/.

[29] srl, 24 consulting. "Grid Making – Sovema." Sovema Group, https://www.sovemagroup.com/product_line/grid-making/.

[30] "Double-Sided Pasting Machine For Lead Acid Battery Production." China Good Quality Geosynthetic Fabric on Sales, http://www.geosynthetic-fabric.com/sale-10356009-double-sided-pasting-machine-for-lead-acid-battery-production.html.

[31] "HydroCure™ Humidity Drying Chamber: Battery Manufacturing." International Thermal Systems, https://www.internationalthermalsystems.com/lead-acid-battery-equipment-manufacturer/humidity-drying-chamber/.

[32] "GROWIN AUTOMATION CO., LTD. :: Home :: Product :: Automatic Battery Manufacturing Equipment." GROWIN AUTOMATION CO., LTD.|COS Assembly Line|Lead Acid Battery|battery Manufacturers|Plate Stacking Machine|VRLA Battery, http://www.growin-auto.com/eng/growin2_1.asp?show=2&kind=4&run=sure&kind2=&kind3=&a2=.

[33] Www.kaelii.com.tw. "Electric Welder & Short Circuit Testing Machine For Automotive Battery, KS-3AC(R) - KAE LII MACHINE MFG CO LTD." , KS-3AC(R) - KAE LII MACHINE MFG CO LTD, http://www.kaelii.com.tw/en/product-109426/Electric-Welder-Short-Circuit-Testing-Machine-For-Automotive-Battery-KS-3ACR.html.

[34] "Lead-Acid Battery." Lead-Acid Batteries, http://hyperphysics.phy-astr.gsu.edu/hbase/electric/leadacid.html.

[35] Pavlov Dečko D. Lead-Acid Batteries: Science and Technology: a Handbook of Lead-Acid Battery Technology and Its Influence on the Product. Elsevier, 2017.

[36] Pavlov, D., and P. Nikolov. "Lead–Carbon Electrode with Inhibitor of Sulfation for Lead-Acid Batteries Operating in the HRPSoC Duty." Journal of The Electrochemical Society, vol. 159, no. 8, 2012, doi:10.1149/2.035208jes.

[37] Garche Jürgen, et al. Lead-Acid Batteries for Future Automobiles. Elsevier, 2017.

Chapter 3 – Experimental Design

A proper test cell and cycling profile that represent SLI lead-acid battery usage in HEV applications are of utmost importance in terms of forming meaningful experimental conclusions. By forming a three-electrode cell setup composed of similar materials used in the design phase of electrode formulation, one can obtain a more accurate representation of the real-world performance. This chapter will begin by providing a brief overview of the three-electrode setup used for the experiment, by describing in detail the procedures followed for preparing and fabricating the various components of the test cell, followed by an outline of the cyclic voltammetry testing parameters used in the experiment. The chapter will then conclude with a description of the teardown sample analysis and calculations to conduct dimensional analysis of the $PbSO_4$ crystals and calculate DCA.

3.1 Test lead-acid cells

Five different paste combinations of NAM type electrodes were fabricated. The test cells were assembled for cycle-life testing. The test cell was a three-electrode cell setup, with a NAM coated lead foil serving as the anode, $Hg/HgSO_4$ as the reference electrode, and platinum foil as the counter electrode. Figure 3.1 shows a CREO model of the three-electrode setup.

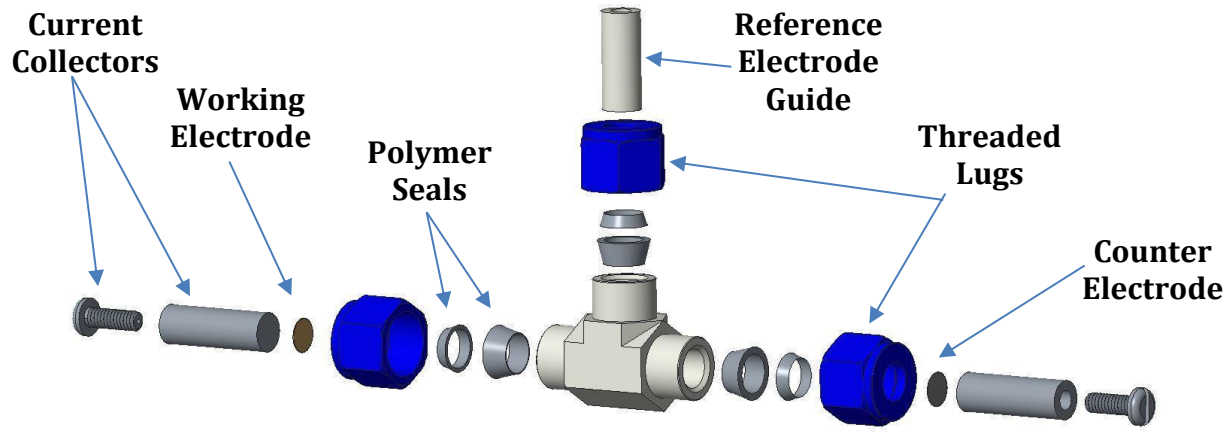

Fig. 3.1 –CREO model of the three-electrode cell setup

3.1.1 NAM Paste Preparation

Five different NAM pastes were created with percentages of active material ranging from 96.55 – 98.00 wt %, as shown in Table 3.1. Sample 1 was created as a baseline, and was only composed of leady oxide and PVDF, with the latter serving as a binding agent. The additive barium sulfate was added to Sample 2, where it serves as a nucleation site for the formation of lead sulfate during operation of the battery. The small size of the barium sulfate particles facilitates the formation of small lead sulfate crystals [38]. A mixture VAN G, a carbon additive, which has been established to reduce the average pore radius of the NAM,

thereby causing a similar effect to the barium sulfate [38], and PBX 135A, a lignin, which adsorbs to the lead surface forming a layer of polyelectrolyte, impeding the formation of a passivating $PbSO_4$ layer, were added to Sample 3[39]. Lastly, two different types of carbon nanotube additives were examined with Samples 4 & 5.

Table. 3.1 – NAM Paste Composition Table by Weight Percentage

Sample Designation	Composition (Wt%)
Sample 1	**Leady Oxide – 98 wt%** **PVDF – 2 wt%**
Sample 2	**Leady Oxide – 97.25 wt%** **Barium Sulfate – 0.75 wt%** **PVDF – 2 wt%**
Sample 3	**Leady Oxide – 96.55 wt %** **Barium Sulfate 0.75 wt%** **VAN G – 0.3 wt %** **PBX 135A – 0.4 wt%** **PVDF – 2 wt %**
Sample 4	**Leady Oxide – 97.6 wt %** **CNT CMC-2 – 0.4 wt %** **PVDF – 2 wt %**
Sample 5	**Leady Oxide – 97.6 wt %** **CNT LS-2 – 0.4 wt %** **PVDF – 2 wt %**

The samples were prepared by mixing the dry components of the pastes together (Fig. 3.2(a)) and mixing them with a Resodyn LabRAM acoustic mixer (Fig. 3.3) with a 60 Hz frequency at 60% intensity for approximately two minutes (Fig. 3.4), in order to create a homogenous mixture of the dry components. Following the brief mixing, the PVDF/NMP mixture was added (Fig. 3.2(b)), and again subjected to acoustic mixing with a frequency of 60 Hz and intensity of 60% for a duration of 5 minutes. Lastly, the remaining NMP was added to the mixture (Fig. 3.2(c)) in 3 equal increments with 5 minutes of acoustic mixing at 60 Hz

frequency, 60% intensity, at each interval until fully mixed (Fig. 3.2(d)). The target weights for each of the individual constituents present within each of the sample mixtures are shown in Table 3.2.

Table. 3.2 – NAM Paste Composition Table by Target Weights

Sample Designation	Target Weights (g)
Sample 1	**Leady Oxide – 5.0000 g** **10 % wt PVDF/NMP – 1.0240 g** **NMP – 2.4830 g**
Sample 2	**Leady Oxide – 5.0000 g** **Barium Sulfate – 0.388 g** **10 % wt PVDF/NMP – 1.0283 g** **NMP – 2.5023 g**
Sample 3	**Leady Oxide – 5.0000 g** **Barium Sulfate – 0.0388 g** **VAN G – 0.0155 g** **PBX 135A – 0.0207 g** **10% wt PVDF/NMP – 1.0357 g** **NMP – 2.5203 g**
Sample 4	**Leady Oxide – 5.0000 g** **CNT CMC-2 – 165.0000 µL** **10% wt PVDF/NMP – 1.0546 g** **NMP – 1.107 g**
Sample 5	**Leady Oxide – 5.0000 g** **CNT LS-2 – 208.5000 µL** **10 % wt PVDF/NMP – 1.0636 g** **NMP – 1.3219 g**

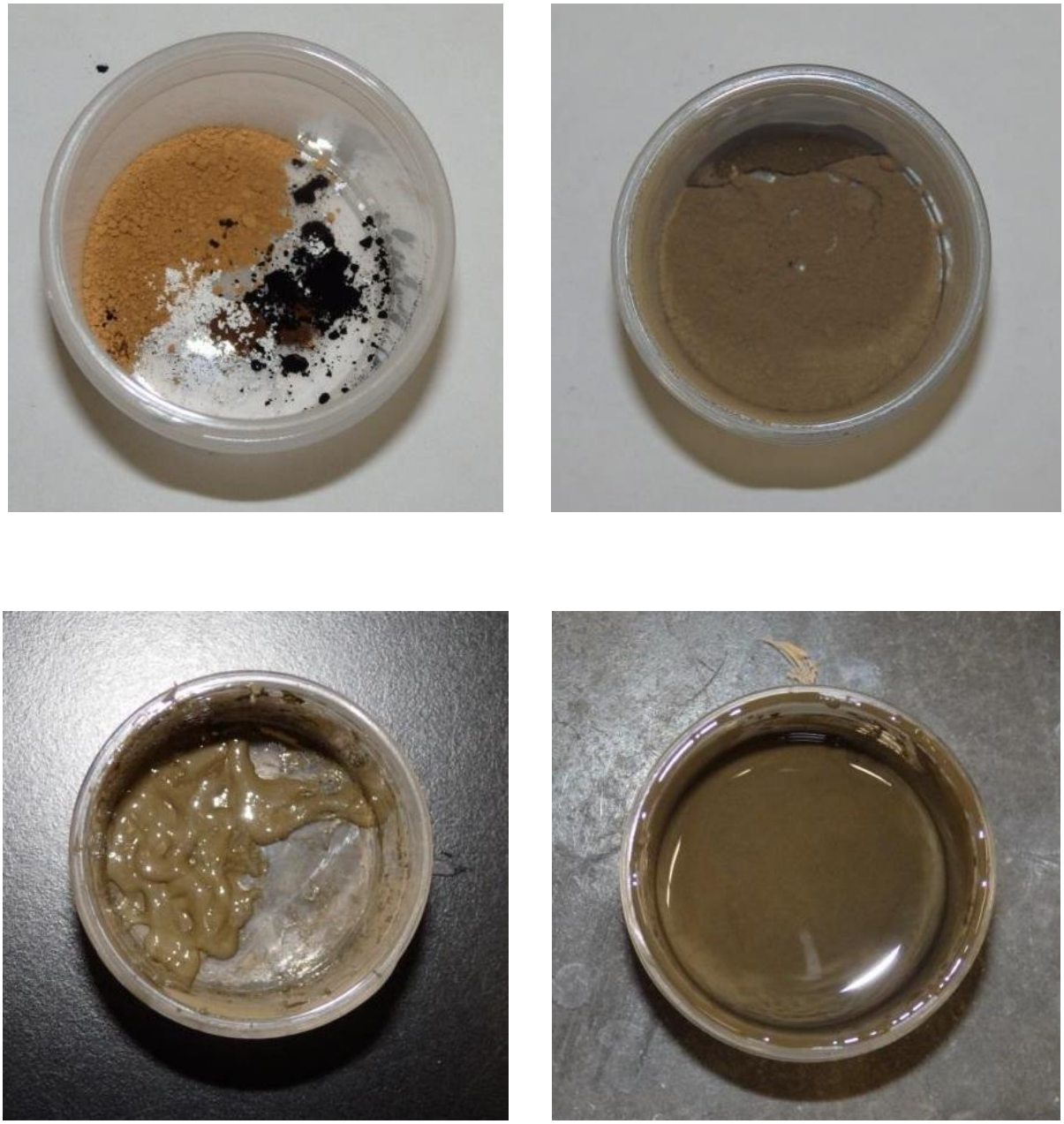

Fig. 3.2 – (a) combination of the dry components of the NAM (b) addition of the PVDF/NMP solution (c) result of the mixing of PVDF/NMP solution and dry components (d) result of mixing the remainder of NMP to PVDF/NMP solution and dry components

Fig. 3.3 – Resodyn LabRAM Acoustic Mixer

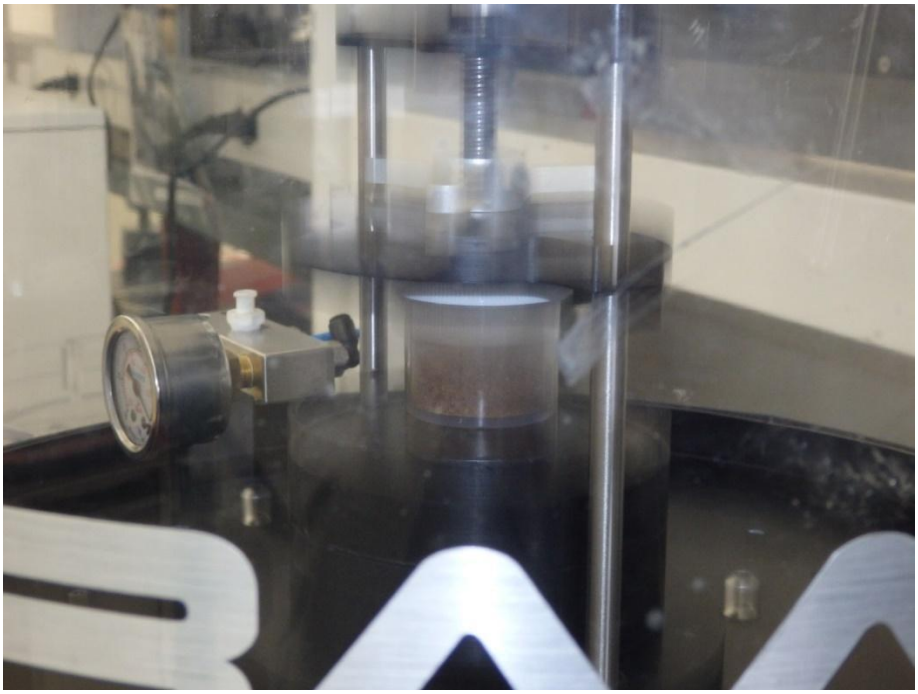

Fig. 3.4 – components were mixed at 60 Hz at 60 % intensity

3.1.2 Lead Foil Preparation

A roughly 4" x 5" section of 0.1 mm thick, 99.95% purity, as rolled temper lead foil supplied from GoodFellow Cambridge Limited, was removed from the roll (Fig. 3.5(a)). The foil was sandwiched with commercial grade aluminum foil and pressed with a hydraulic press to remove any induced wrinkles during the sectioning process (Fig. 3.5(b)). The foil was then affixed to a glass sheet with tape (Fig. 3.5(c)). A scotch bright pad was utilized to abrade the coating surface to aid in better adhesion of the NAM (Fig. 3.5(d)). The sample was then cleaned with Kimtech wipes and methanol.

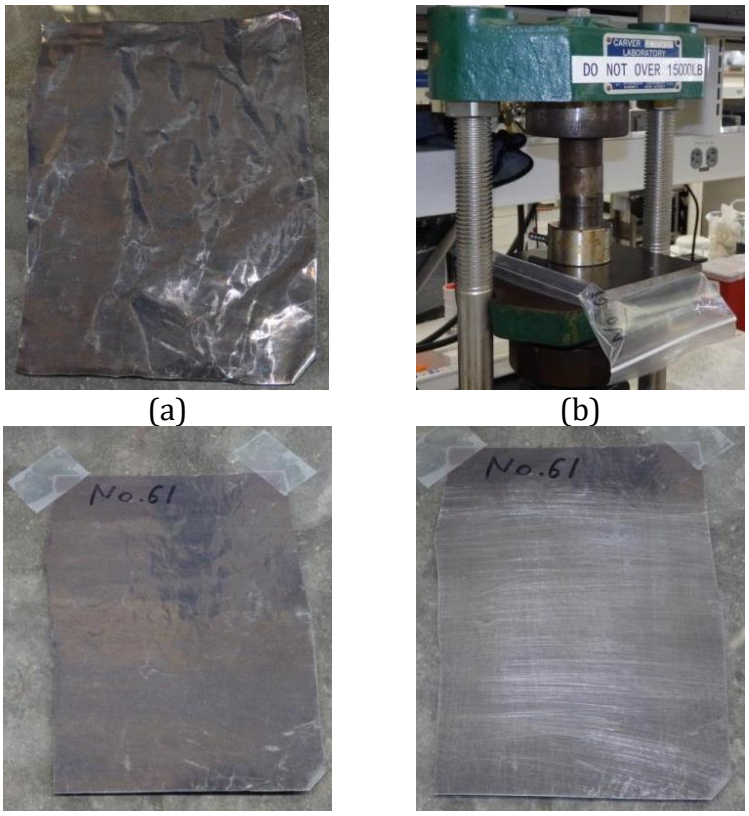

(a) (b)

(c) (d)

Fig. 3.5 –(a) section of foil removed from roll (b) section sandwiched between aluminum sheets and plastic bag and hydraulically pressed to remove wrinkles (c) as pressed condition of the section of foil (d) abraded condition of foil sample

3.1.3 NAM Paste Coating Procedure

A 1-8 mils 8 path applicator supplied from Precision Gage & Tool Co. was utilized to apply an even coating of the NAM at 8 mils thickness. The NAM paste mixture was evenly dispersed along the 8 mils side in the manner shown in Figure 3.6(a). The path applicator was slowly pulled with a roughly constant velocity, in order to apply an even coating. A representative example of the freshly applied NAM paste is shown in Figure 3.6(b).

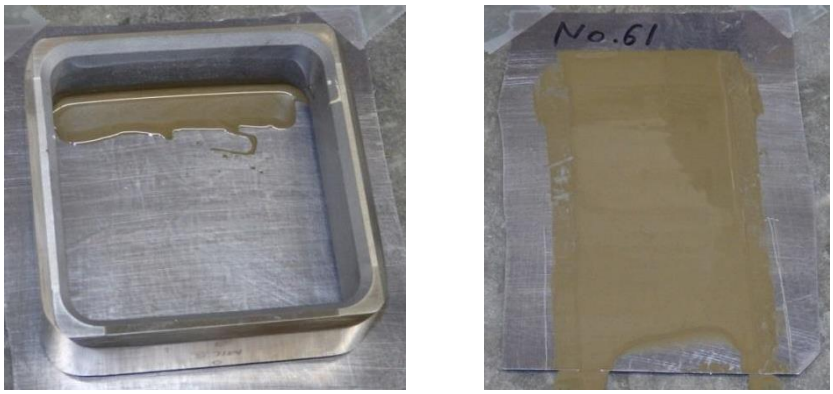

Fig. 3.6 – (a) paste from Fig. was transferred to the 1-8 mils 8 path applicator (b) result of the NAM applied to the abraded Pb foil

The samples were then carefully transported to a Thermo Scientific Lindberg Blue M furnace with a temperature set value of 50°C, to evaporate the NMP solvent until dry, as shown in Figure 3.7.

Fig. 3.7 -Thermo Scientific Lindberg Blue M Furnace

3.1.4 Working Electrode Fabrication

The dried coated foil was sandwiched between commercial grade aluminum foil and hydraulically pressed with 5 tons of pressure for 10 seconds. Following the pressing process, a folded sheet of white – 92 bright laser finish printer paper was then utilized, in conjunction with a 7/16" punch press and ball-peen hammer (Fig. 3.8), to punch out the electrode (Fig. 3.9).

Fig. 3.8 – Electrode Fabrication Setup

Fig. 3.9 -Representative Image of Working Electrode

3.1.5 Counter Electrode Fabrication

A 0.025 mm thick, 99.9% purity platinum foil supplied via Alfa Aesar, was fabricated similarly to the working electrode, by using a folded sheet of white – 92 bright laser finish printer paper, in conjunction with a 7/16" punch press, and ball-peen hammer, to punch out two electrodes, shown in Figure 3.10.

Fig. 3.10 – Two 7/16" Pt counter electrodes

3.1.6 Current Collector Fabrication

A 0.5" diameter rod of a Nichrome alloy was machined into roughly 1.5" long sections (Fig. 3.11). The rods were then tapped to allow the insertion of a 7/8" threaded screw to be inserted into the rod. This alloy was chosen for its excellent sulfuric acid corrosion resistance and acceptable electrical conductivity. 8 rods in total were fabricated.

Fig. 3.11 – Representative NiCr Alloy Current Collectors

3.1.7 Electrolyte Preparation

Lab grade sulfuric acid and distilled water were utilized to prepare 1 L of an electrolyte solution with a specific gravity of 1.28 g/mL. 15 g/L of solid sodium sulfate was then added to the solution.

3.1.8 Test Cell Design

The test cell is a three-electrode cell, shown in Figure 3.12, which uses a Bio-Logic RE-2CP $Hg/HgSO_4$ electrode as a reference, the NAM pasted lead foils as the working electrode, and platinum as the counter electrode. A Swagelok cell was chosen due to availability and its chemical resistance to the sulfuric acid electrolyte.

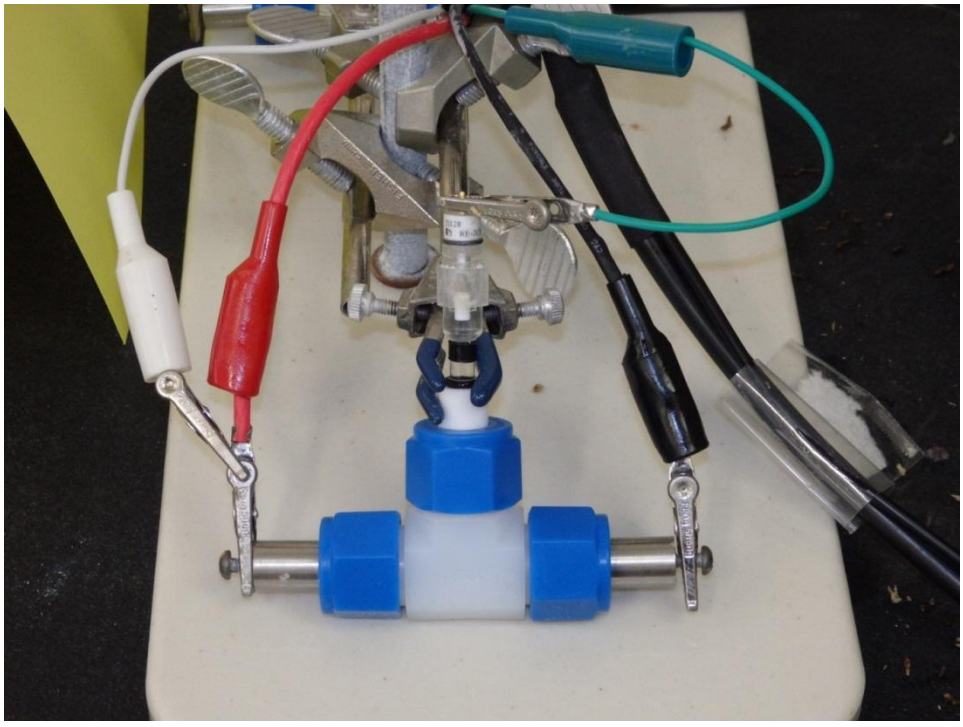

Fig. 3.12 – Working electrode (red lead), sensing electrode (white lead), $Hg/HgSO_4$ reference electrode (green lead), and Pt counter electrode (black lead)

3.2 Cyclic Voltammetry Testing Parameters

An Arbin BT-2000 battery tester (Fig. 3.13) was utilized to run cyclic voltammetry testing of the cells. Polarized between -0.70 V and -1.30 V (vs. Hg/Hg_2SO_4 reference electrode) at a scan rate of 5 $mV.s^{-1}$. The cells were then cycled for 60 cycles, 300 cycles, 600 cycles, and 900 cycles. The cells were cycled for 60 cycles and then resting for various time periods in order to study the coarsening effect over time. The time increments were 1 hour, 6 hours, 12 hours, 36 hours, and 96 hours. The testing steps are as follows:

1. Measure OCV for 60 seconds taking a data point once every second.
2. Run from OCV to -0.95 V at a scan rate of 0.5 mV/s taking a data point once every second or once every dV of 1mV, whichever happens sooner.
3. -0.95 V to -1.3V at a scan rate of 5 mV/s taking a data point once every second or once every dV of 1mV, whichever happens sooner.
4. -1.3 V to -0.7 V at a scan rate of 5 mV/s taking a data point once every second or once every dV of 1 mV, whichever happens sooner.
5. -0.7 V to -1.3 V at a scan rate of 5 mV/s taking a data point once every second or once every dV of 1 mV, whichever happens sooner.

Fig. 3.13 – Arbin BT-2000 Battery Tester

3.3 Teardown Sample Analysis

3.3.1 Rinsing & Drying of the Working Electrodes

A set of tweezers was used to carefully separate the working electrodes from their current collectors. The working electrodes were then carefully placed into a petri dish containing lab grade methanol. The samples were left in the methanol for approximately 90 seconds. The tweezers were again used to slowly lift the working electrodes from the petri dish and set on a glass plate. The glass plate containing the rinsed electrodes was then placed in a Thermo Scientific Lindberg Blue M furnace at 50°C until dry.

3.3.2 Scanning Electron Microscopy

A Jeol JSM-6460LV Scanning Electron Microscope was utilized to ascertain high magnification high resolution images of the lead sulfate crystals. Images were taken at 1.5 KX, 2.5 KX, 5 KX, 7.5 KX, and 10 KX magnification for each sample set. Additional images were taken in three different areas of the samples for additional crystals for measurement. The additional images were taken at 1.5 KX, 2.5 KX, and 5 KX magnifications. The equipped Oxford Inca X-Sight Si drifted lithium energy dispersive spectrometer was used to characterize the suspected lead sulfate crystals. Representative characterization of the elemental constituents present within the $PbSO_4$ crystals is shown in Figures 3.14 & 3.15.

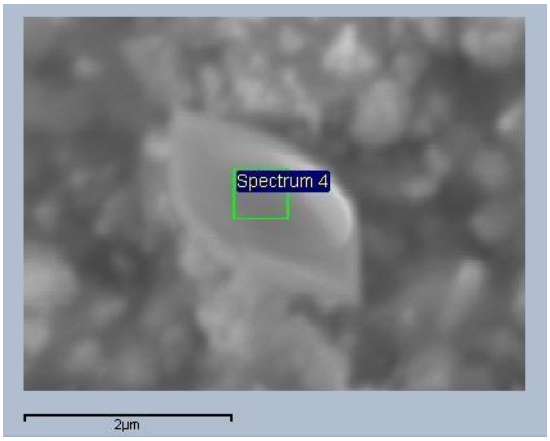

Fig. 3.14 – Scanning Electron Micrograph of $PbSO_4$ Crystal

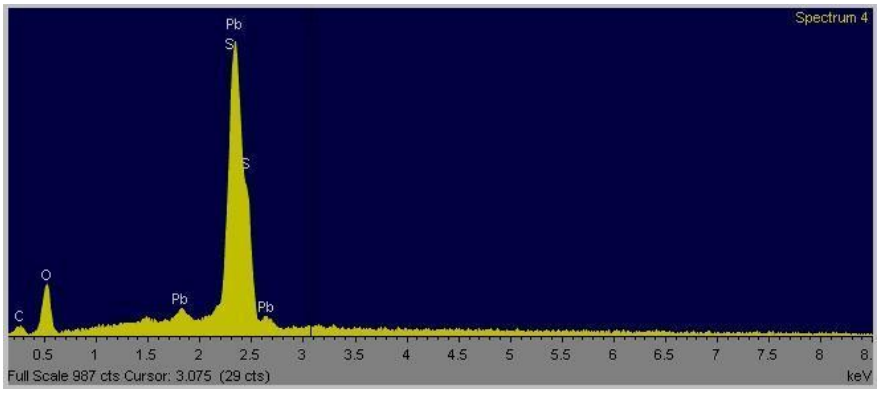

Fig. 3.15 – EDS Elemental Spectrum of $PbSO_4$ Crystal

3.4 Calculations

3.4.1 Dimensional Analysis of $PbSO_4$ Crystals

ImageJ image processing and analysis software was used to measure the major and minor diameters of the lead sulfate crystals. Ten crystals per sample were analyzed. Due to the complex faceted nature of the lead sulfate crystals, the area was approximated as a diamond per EQ.5, where A is equal to area, D_{major} is equal to the major diameter, and D_{minor} is equal to the minor diameter. A representative image of the dimensional analysis is shown in Figure 3.14.

$$\mathbf{A = (D_{major} * D_{minor}) / 2} \qquad \mathbf{(EQ.\ 5)}$$

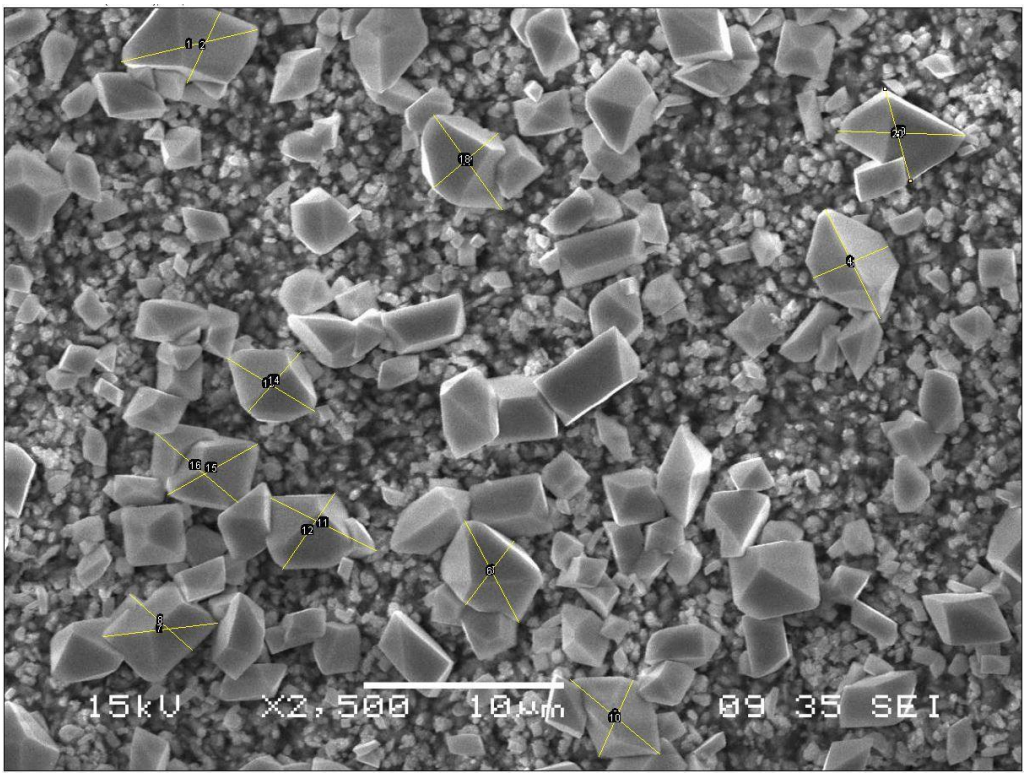

Fig. 3.16 – Representative Scanning Electron Micrograph of Dimensional Analysis of Lead Sulfate Crystals

3.4.2 Dynamic Charge Acceptance Calculation

OriginPro 2016 Data Analysis and Graphing Software was used to evaluate the CV curves generated from cycling the three-electrode cell. The minimum and maximum functions were applied to the data set in the area of the CV curve that represented the reduction of $PbSO_4$ to Pb for each sample. The maximum function was applied to the edges of the estimated total reduction reaction, in order to determine the edges of the envelope for the voltage range for the onset (E2) and end (E1) of the reduction reaction. The integration function was used to ascertain the area under the curves between the previously determined voltage window. Microsoft Excel was then used to calculate dynamic charge acceptance using Equation 6, which involves taking the $PbSO_4$ to Pb reduction peak area divided by the potential difference between the onset and end of the reduction reaction, as evident in Figure 3.15.

$$\textbf{DCA = Reduction Peak Area / } (E_2 - E_1) \qquad \textbf{(EQ. 6)}$$

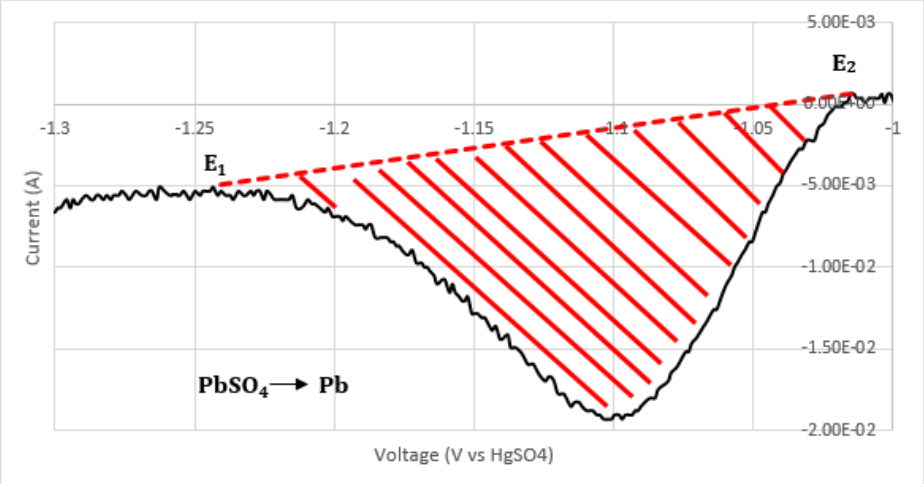

Fig. 3.17 – Representative DCA Calculation

Chapter 3 References Cited

[38] Pavlov, D., et al. “Influence of Expander Components on the Processes at the Negative Plates of Lead-Acid Cells on High-Rate Partial-State-of-Charge Cycling. Part II. Effect of Carbon Additives on the Processes of Charge and Discharge of Negative Plates.” Journal of Power Sources, vol. 195, no. 14, 2010, pp. 4444–4457., doi:10.1016/j.jpowsour.2009.12.132.

[39] Senthil Kumar P, et al. “Influence of Carbon and Interaction of Carbon and Lignosulfonate on Dynamic Charge Acceptance of Flooded (Enhanced) Lead Acid Batteries.” International Journal of Science and Research, vol. 7, no. 3, 2018, pp. 1940 – 1946., doi:10.21275/ART20181171

Chapter 4 – Experimental Results & Formal Discussion

This chapter will address the experimental results obtained during the various CV testing conducted using the 3-electrode cell. A full discussion of the $PbSO_4$ crystal growth kinetics will be addressed, with a particular emphasis on the effects of coarsening with respect to time, and the number of cycles endured, as it pertains to $PbSO_4$ crystal size and dynamic charge acceptance. After the initial discussion of the effects of coarsening and cycling on the $PbSO_4$ crystal growth kinetics, a discussion concerning the impacts of the NAM additives, as well as the form of the carbon additives will follow. Lastly, a discussion regarding the various challenges the were encountered during the experiment, which may have accounted for observed variances from theoretical expectations, as well as possible mitigation strategies, should the work herein be replicated or expanded upon in the future.

4.1 Results from electrochemical testing

This section will first discuss changes in average crystal size and area for samples that had been subjected to 60 cycles, which was followed by coarsening times varying from 1 to 96 hours. The following section will discuss changes in average crystal size and area for samples that had been subjected to cycles ranging from 60 to 900 cycles. The last section will discuss changes in average DCA, which were calculated from CV curves for each of the samples at 5, 12, 24, 36, 48, & 60 cycles.

The leady oxide (LO), leady oxide plus barium sulfate (LOBS), and Mix 54 samples were prepared and tested together. The CNT samples, CNT CMC-2 and CMC LS-2, were prepared and tested together after the initial set, where several potential mitigation strategies for some of the challenges experienced in the first sample set, were employed.

4.1.1 Crystal Size as a Function of Time

Analysis of the average crystal size (length) after the samples were left to coarsen for 1 hour post-cycling, revealed a larger crystal size for the LOBS and Mix 54 samples relative to the LO sample, which was most likely attributed to the additives present within the NAM, serving as nucleation sites for the $PbSO_4$ crystals. After 12 hours of coarsening, a decrease in crystal size of roughly 20% and 38% relative to the 1 hour coarsened samples for both the LOBS and Mix 54 samples, respectively was observed, as evident in Table 4.1. The LO sample, on the other hand, was found to have slightly increased by roughly 10%.

Table. 4.1 – Crystal Size (Length) Table for 60 Cycles 1- & 12-hour Coarsening Times

Sample Designation	Average Crystal (length), µm		% Change
	1 Hour Coarsening	12 Hour Coarsening	1 Hour – 12 Hour Coarsening
LO	2.53	2.78	9.88
LOBS	3.89	3.12	-19.79
Mix 54	3.69	2.28	-38.21

Scanning electron micrographs comparing the LO, LOBS, & Mix 54 samples, after 1 hour and 12 hours of coarsening time, are shown in Figure 4.1. The decrease in average crystal size (length) for the LOBS and Mix 54 samples, could possibly be explained by the presence of fewer, larger crystals after 1 hour of coarsening time, relative to the more numerous, smaller crystals after 12 hours of coarsening time, which may have been attributed to differences in NAM additive homogeneity between the samples. The homogeneity of the samples was one of the challenges, which may have attributed to variances from theoretical expectations, and will be elaborated near the end of the chapter.

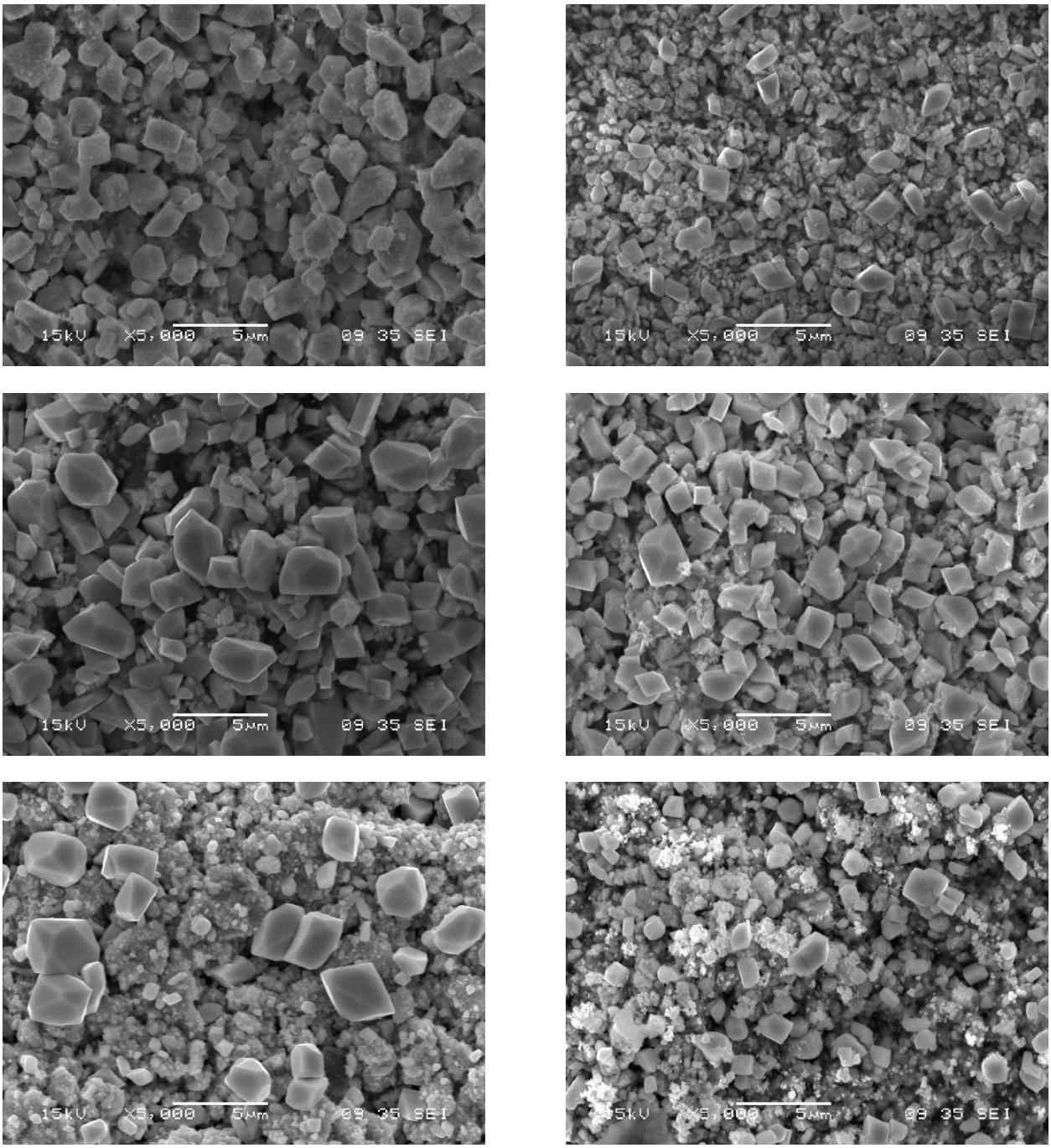

Fig. 4.1 – Comparisons 60 Cycles 1 Hour & 12 Hours, LO (Top), LOBS (Center) & Mix54 (Bottom)

Examination of the average crystal size (length) for the CNT samples revealed a significantly smaller crystal size relative to the non-CNT samples, both for the 1-hour and the 12-hour coarsening times, as evident in Table 4.2. Furthermore, the percent change in crystal size was also substantially larger relative to the non-CNT samples. This is consistent with theoretical expectations, where the CNT additives increase the electrochemical activity of the NAM, as well as restrain $PbSO_4$ crystal growth.

Table. 4.2 – CNT Crystal Size (Length) Table for 60 Cycles 1- & 12-hour Coarsening Times

Sample Designation	Average Crystal (length), µm		% Change
	1 Hour Coarsening	12 Hour Coarsening	1 Hour – 12 Hour Coarsening
CNT CMC-2	1.14	2.44	114.04
CNT LS-2	0.98	1.78	81.63

Scanning electron micrographs comparing the CNT CMC-2 and CNT LS-2 samples after 1 hour and 12 hours of coarsening time, are shown in Figure 4.2. The number of $PbSO_4$ crystals observed was significantly less compared to the non-CNT samples, and the crystals appeared less faceted, suggesting that the crystals are more amorphous, and thus theoretically will more readily dissolve.

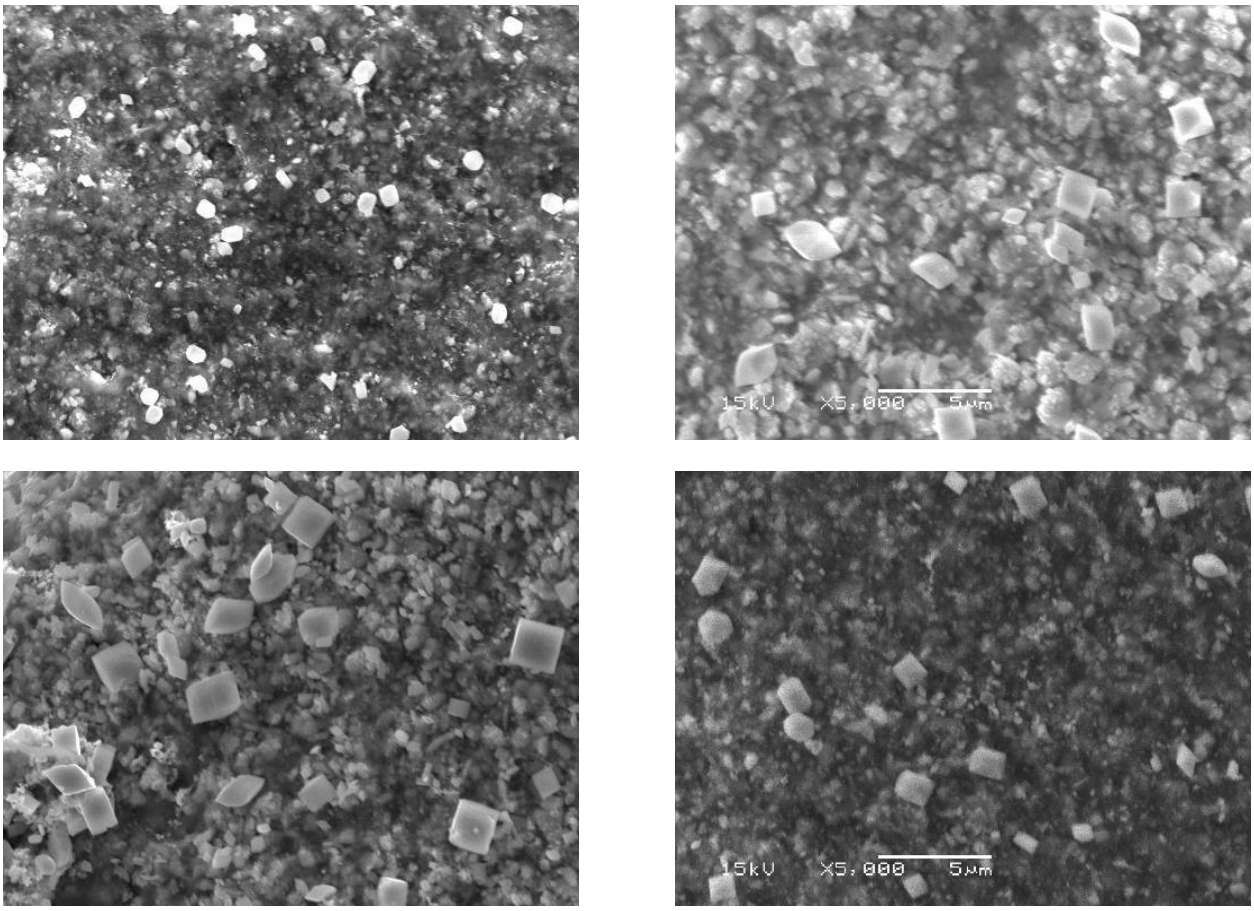

Fig. 4.2 – CNT Comparisons 60 Cycles 1 Hour & 12 Hours, CNT CMC-2 (Top) & CNT LS-2 (Bottom)

An overall graphical representation of the average $PbSO_4$ crystal size (length), as a function of coarsening time is shown in Figure 4.3. The first set of samples (LO, LOBS, & Mix

54) evaluations were conducted for 1, 12, and 36 hours of coarsening time. After 36 hours of coarsening time, the integrity of the samples due to observed challenges precluded subsequent evaluations. The second set of samples (CNT CMC-2 & CNT LS-2), due to time constraints, were conducted for 1, 12, and 96 hours, in order to ascertain a general understanding of the effects on $PbSO_4$ crystal size for both short and long coarsening times.

Although the values vary between the samples, the general trend of an increase in average crystal size (length) with respect to coarsening time was observed. The growth kinetics of the $PbSO_4$ crystals was significantly affected by the presence of different NAM additives relative to the LO control sample.

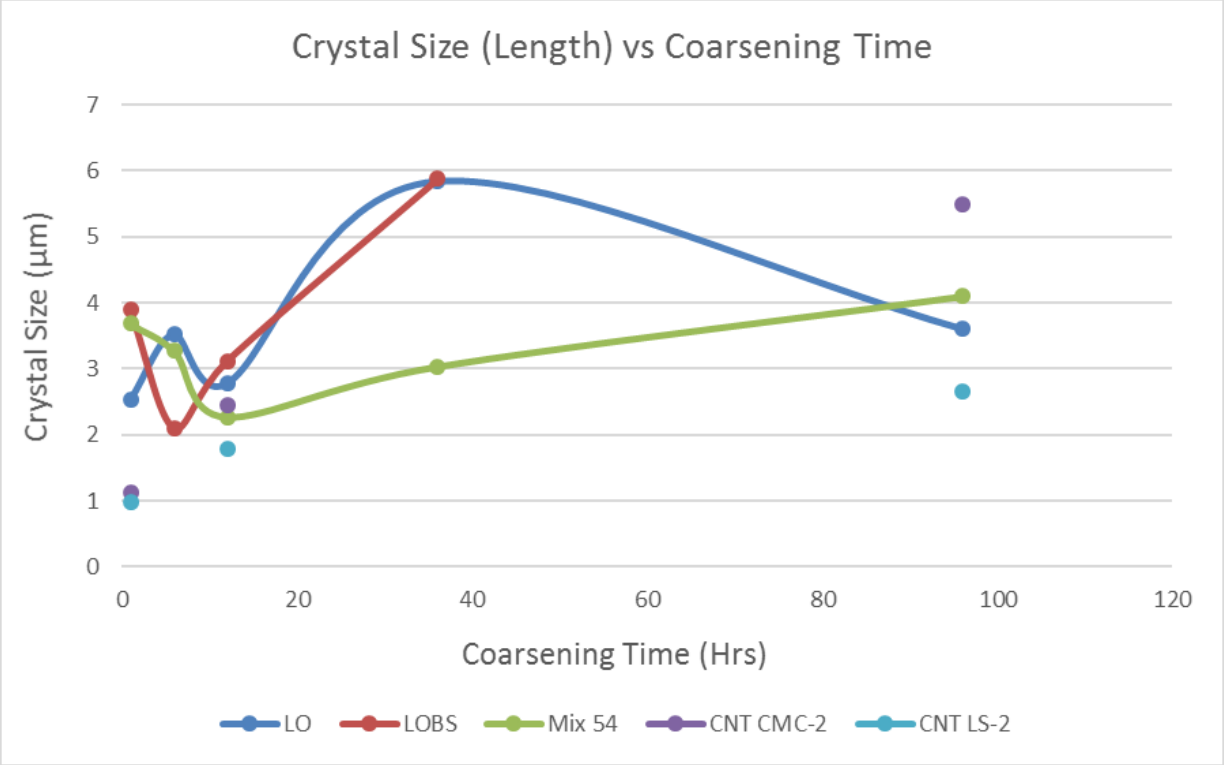

Fig. 4.3 – Crystal Size (Major Diameter) vs Coarsening Time (Hrs)

Comparing the average crystal size (length) after the samples were left to coarsen for 36 hours post-cycling to the 1 hour coarsened samples, revealed a substantial increase in crystal size for the LO sample, and a moderate increase in crystal size for the LOBS sample as shown in Table 4.3. The observations in crystal size are in line with theoretical expectations, where the barium sulfate additive served to promote higher $PbSO_4$ crystal nucleation rates, in the LOBS sample. The Mix 54 samples was found to slightly decrease in average crystal size (length) relative to the 1 hour coarsened sample; However, the average crystal size (length) was found to have increased relative to the 12 hour coarsened sample, and further increased after 96 hours of coarsening time. A similar trend of increase in average crystal size (length) was observed, although delayed, perhaps as a function of the carbon additives.

Table. 4.3 – Crystal Size (Length) Table for 60 Cycles 1- & 36-hour Coarsening Times

Sample Designation	Average Crystal (length), µm		% Change
	1 Hour Coarsening	36 Hour Coarsening	1 Hour – 36 Hour Coarsening
LO	2.53	5.84	130.83
LOBS	3.89	5.89	51.41
Mix 54	3.69	3.04	-17.62

Visual examination of the scanning electron micrographs, which show the comparisons of the LO, LOBS, & Mix 54 samples that were subjected to 60 cycles followed by a coarsening time of 36 hours, revealed the fewest and largest faceted $PbSO_4$ crystals of all the samples, as evident in Figure 4.4. More $PbSO_4$ crystals, with relatively equal major and minor diameters were observed in the LOBS sample relative to the LO sample, which was likely a function of the barium sulfate serving as nucleation sites. The $PbSO_4$ crystals present on the Mix 54 sample were significantly more numerous, smaller, and were less faceted than both of the LO and LOBS samples, which further illustrates the carbon additive's role in impeding crystal growth and enhancing the electrochemical activity of the NAM.

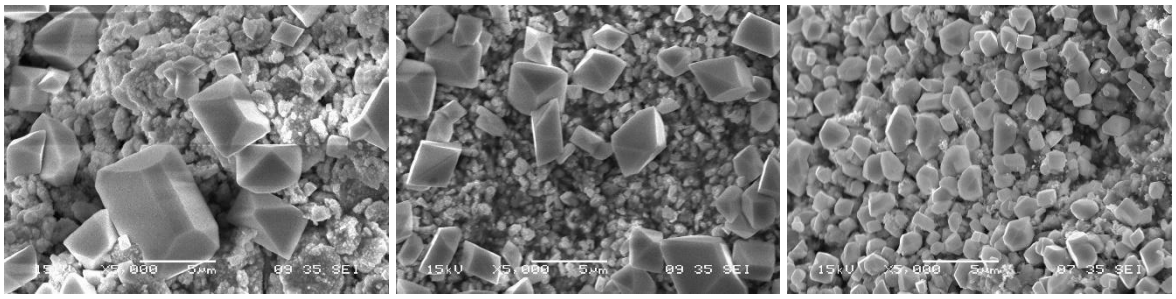

Fig. 4.4 – Comparisons 60 Cycles 36 Hours, LO (Left), LOBS (Center), & Mix 54 (Right)

The average $PbSO_4$ crystal size (length) was plotted as a function of the square-root of coarsening time, for the LO, LOBS, & Mix 54 samples is shown in Figure 4.5. It was suspected that the crystal size as a function of time would appear parabolic in nature, and therefore would appear linear when plotted as a function of the square-root of time. However, the resultant trendlines did not align with theoretical expectations. The poor correlation of crystal size (length) with respect to the square-root of coarsening time, was most likely attributed to a multitude of challenges encountered during the testing of the first set of samples.

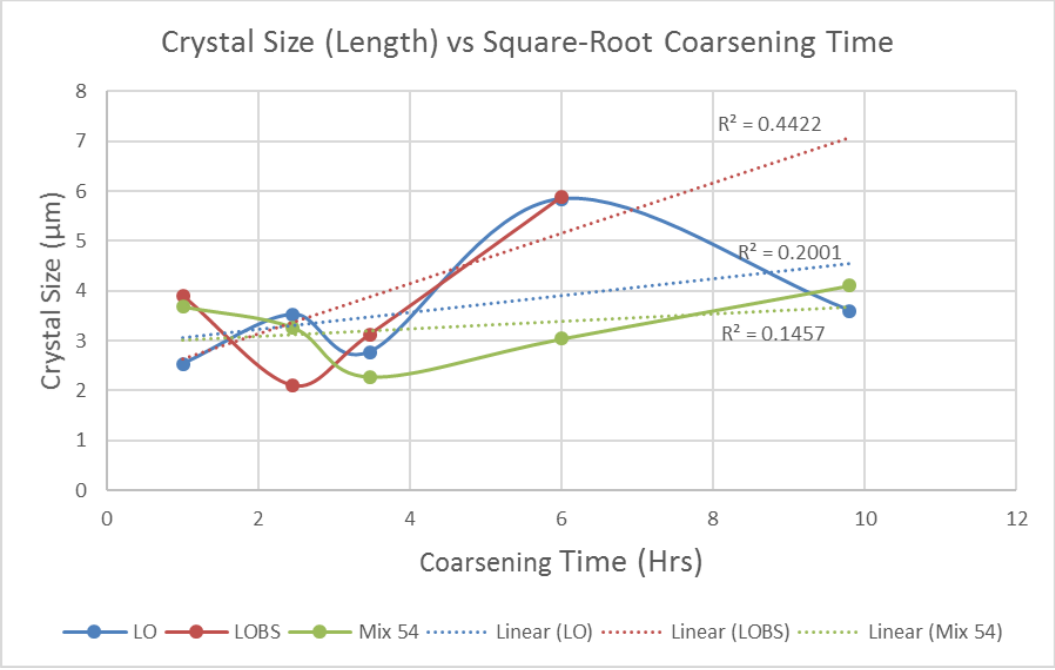

Fig. 4.5 – Crystal Size (Length) vs Square-Root Coarsening Time (Hrs) – LO, LOBS, & Mix 54

Analysis of the average crystal size (length) revealed increases of roughly 382% and 173% between the 1-hour and 96-hour coarsening times for both the CNT CMC-2 and CNT LS-2 samples, respectively, as evident in Table 4.4. The average crystal size (length) at 96

hours of coarsening for both of the CNT samples, were smaller than both the LO and LOBS samples at 36 hours of coarsening, further demonstrating the carbon additives effects on crystal size.

Table. 4.4 – CNT Crystal Size (Length) Table for 60 Cycles 1- & 96-hour Coarsening Times

Sample Designation	Average Crystal (length), µm		% Change
	1 Hour Coarsening	96 Hour Coarsening	1 Hour – 96 Hour Coarsening
CNT CMC-2	1.14	5.49	381.58
CNT LS-2	0.98	2.67	172.45

Scanning electron micrographs showing the comparisons of the CNT samples that were subjected to 60 cycles followed by a coarsening time of 1 hour with the CNT samples that had been subjected to 60 cycles followed by a coarsening time of 96 hours, for the CNT CMC-2 and CNT LS-2 samples, are shown in Figure 4.6. Fewer $PbSO_4$ crystals were observed relative to the 36 hour coarsened non-CNT samples. Additionally, the crystals appeared morphologically similar to the 1 hour and 12 hour CNT samples, which were less faceted, suggesting again that the crystals are more amorphous, and thus theoretically will more readily dissolve.

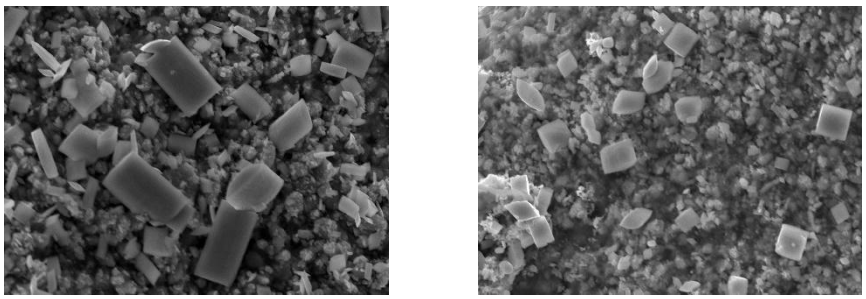

Fig. 4.6 – CNT Comparisons 60 Cycles 96 Hours, CNT CMC-2 (Left) & CNT LS-2 (Right)

Similar to the non-CNT samples, the average $PbSO_4$ crystal size (length) was plotted as a function of the square-root of coarsening time, for the CNT CMC-2 and CNT LS-2 samples as shown in Figure 4.7. Both samples were found to exhibit linearity, which aligns with theoretical assumptions. Mitigation strategies for some of the challenges observed with the first set of samples were employed, which most likely accounted for the expected result.

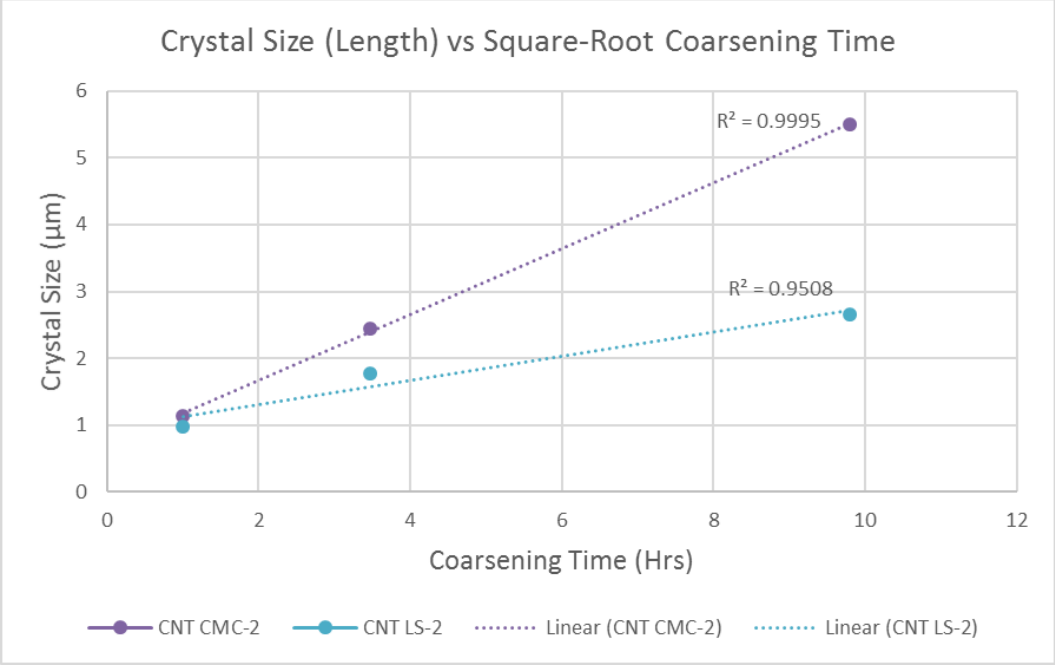

Fig. 4.7 – Crystal Size (Length) vs Square-Root Coarsening Time (Hrs) – CNT CMC-2 & CNT LS-2

In addition to the evaluation of average crystal size conducted via measurements of the major diameter length, analysis of crystal size via area was also conducted. Graphical representations of the average $PbSO_4$ crystal size (area), as a function of coarsening time is shown in Figure 4.8.

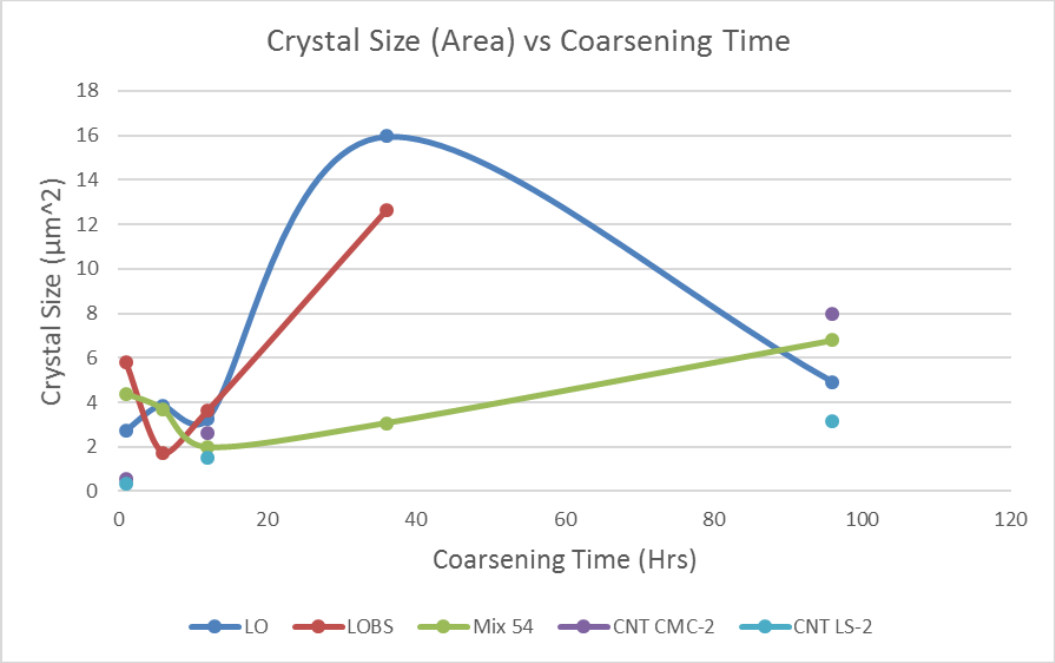

Fig. 4.8 – Crystal Size (Area) vs Coarsening Time (Hrs)

Analysis of the average crystal size (area) for 1, 12, and 36 hour coarsening times for the LO, LOBS, & Mix 54 samples revealed a similar trend observed with the average crystal size (length), as shown in Table 4.5. The comparison of percentage changes in crystal size (area) between 1 and 12 hour coarsened samples were roughly twice the changes observed with the average crystal (length), which indicated that the crystals had similar major and minor diameters. Comparisons of the percentage changes in crystal size (area) between the 1 and 36 hour coarsening, were roughly four times as much for the changes observed for

average crystal (length) for the LO sample, and twice as much for the LOBS sample. The crystal size (area), actually increased after 36 hours of coarsening relative to the 1 hour coarsening for the Mix 54 sample, which decreased its percentage change in crystal size (length) in that same timeframe.

Table. 4.5 – Crystal Size (Area) Table for 60 Cycles 1- & 12-hour Coarsening Times

Sample Designation	Average Crystal (Area), μm^2			% Change	
	1 Hour Coarsening	12 Hour Coarsening	36 Hour Coarsening	1 Hour – 12 Hour Coarsening	1 Hour – 36 Hour Coarsening
LO	2.73	3.24	15.96	18.68	484.62
LOBS	5.83	3.63	12.62	-37.74	116.47
Mix 54	4.39	1.97	6.79	-55.13	54.67

The average $PbSO_4$ crystal size (area) was plotted as a function of the square-root of coarsening time, for the LO, LOBS, & Mix 54 samples as shown in Figure 4.9. Similar to the evaluation of the crystal size (length), it was suspected that the crystal size as a function of time would appear parabolic in nature, and therefore would appear linear when plotted as a function of the square-root of time. However, the resultant trendlines, once again, did not align with theoretical expectations. The poor correlation of crystal size (area) with respect to the square-root of coarsening time, due to the same samples evaluated in crystal size (length), was again most likely attributed to a multitude of challenges encountered during the testing of the first set of samples.

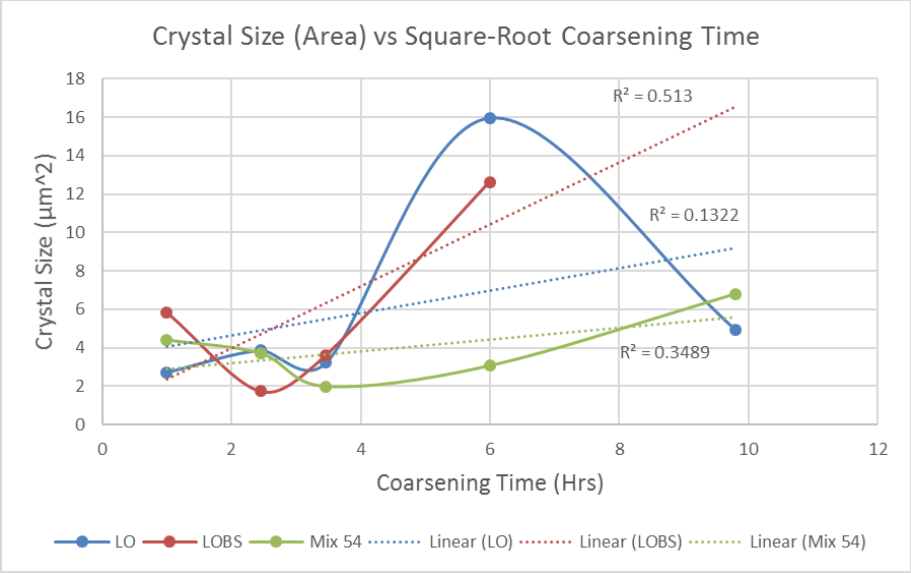

Fig. 4.9 – Crystal Size (Area) vs Square-Root Coarsening Time (Hrs) – LO, LOBS, & Mix 54

Analysis of the average crystal size (Area) for the 1, 12, and 96 hour coarsening times for the CNT CMC-2 and CNT LS-2 samples, revealed a similar trend observed with the average crystal size (length), as well as similar dramatic changes observed for the non-CNT sample crystal size (area), as shown in Table 4.6. The comparison of percentage changes in crystal size (area) between 1 and 12 hour coarsened samples, was roughly 3 and 4.5 times larger relative to changes in the crystal size (length) for the same timeframe. The comparison of percentage changes in crystal size (area) between 1 and 96 hour coarsened samples, was roughly 3 and 5 times larger relative to changes in the crystal size (length) for the same timeframe.

Table. 4.6 – CNT Crystal Size (Area) Table for 60 Cycles 1- & 12-hour Coarsening Times

Sample Designation	Average Crystal (Area), µm²			% Change	
	1 Hour Coarsening	12 Hour Coarsening	96 Hour Coarsening	1 Hour – 12 Hour Coarsening	1 Hour – 96 Hour Coarsening
CNT CMC-2	0.58	2.61	7.96	350.00	1,272.41
CNT LS-2	0.32	1.49	3.14	365.63	881.25

Similar to the non-CNT samples, the average $PbSO_4$ crystal size (area) was plotted as a function of the square-root of coarsening time, for the CNT CMC-2 and CNT LS-2 samples as shown in Figure 4.10. As with the crystal size (length) for the CNT samples, the crystal size (area) exhibited linearity, which aligns with theoretical assumptions.

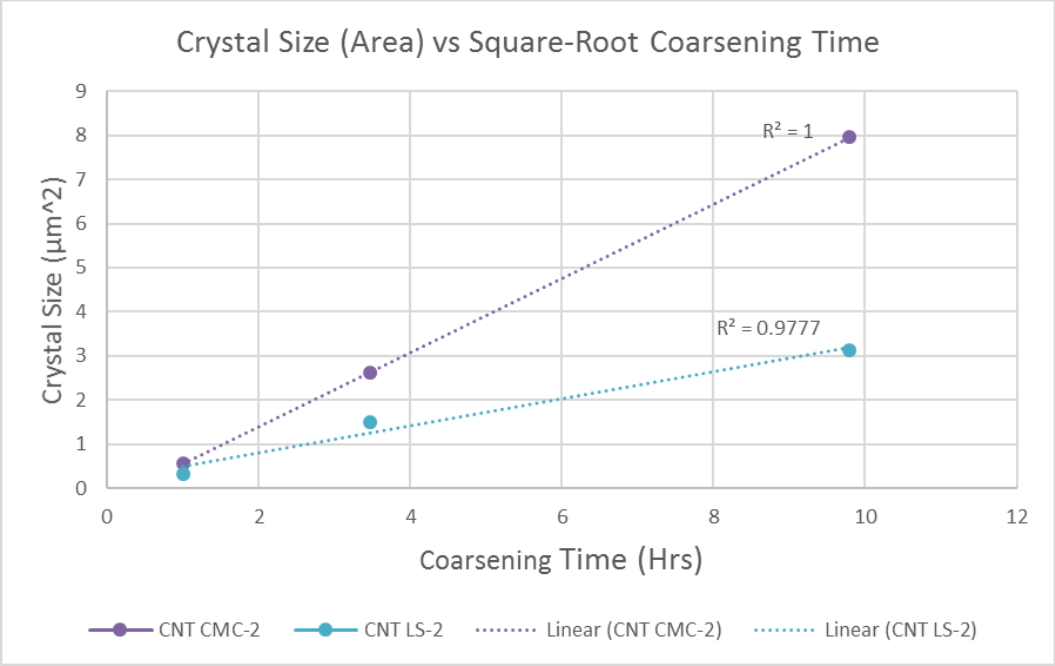

Fig. 4.10 – Crystal Size (Area) vs Square-Root Coarsening Time (Hrs) – CNT CMC-2 & CNT LS-2

4.1.2 Crystal Size as a Function of Cycling

Analysis of the average crystal size (length) after the samples were subjected to 60, 300, and 600 cycles, revealed an initial increase in the average crystal sizes for the LO and LOBS samples, and a slight decrease in the average crystal size for the Mix 54 sample from the 60 – 300 cycles, as shown in Table 4.7. Following the initial increase observed with the LO and LOBS samples, the LO sample was observed to decrease in average crystal size between 300 and 600 cycle samples. The LOBS sample, similar to the initial observations, was found to have a significant increase in average crystal size, between the 300 – 600 cycles. After the initial decrease in average crystal size observed for the Mix 54 sample from the 60 – 300 cycles, an increase in average crystal size occurred between 300 – 600 cycles.

Table. 4.7 – Average Crystal Size (Length) Table for 60, 300, & 600 Cycles

Sample Designation	Average Crystal (Length), µm		
	60 Cycles	300 Cycles	600 Cycles
LO	2.14	4.22	2.42
LOBS	2.21	2.53	9.47
Mix 54	4.34	3.86	4.79

Analysis of the percent changes in average crystal size (length) after the samples were subjected to 60, 300, and 600 cycles, revealed a substantial increase for the LO sample, with roughly 97% change relative to the initial average crystal size. The LOBS and Mix 54 samples revealed more moderate changes in average crystal size of roughly a 15% increase and 11% decrease, respectively, as shown in Table 4.8. Following the initial substantial increase observed with the LO sample, the LO sample was observed to decrease roughly 43% in average crystal size between 300 and 600 cycle samples, which still resulted in a roughly 13% increase in average crystal size. The LOBS sample exhibited a dramatic percent change

in average crystal size between 300 – 600 cycles, growing roughly 274%, culminating in a total percent change of nearly 329% relative to the initial average crystal size. After the initial decrease in average crystal size observed for the Mix 54 sample from the 60 – 300 cycles, an increase in average crystal size occurred between 300 – 600 cycles. The Mix 54 exhibited moderate percent changes in average crystal size throughout the cycling duration, growing roughly 10% relative to the initial average crystal size.

Table. 4.8 – Percent Change in Intercycle Average Crystal Size (Length) Table

Sample Designation	% Change in Average Crystal (Length), µm		
	60 – 300 Cycles	300 – 600 Cycles	60 – 600 Cycles
LO	97.20	-42.65	13.08
LOBS	14.48	274.31	328.51
Mix 54	-11.06	24.09	10.37

Scanning electron micrographs, showing the differences in $PbSO_4$ crystal growth kinetics between the LO, LOBS, & Mix 54 samples after 60, 300, and 600 cycles, are shown in Figure 4.11. The untransformed NAM appeared visually different in comparison to the coarsened samples, which may have been attributed to some of the challenges encountered during the experiment, specifically the corrosion of the current collectors, and delamination of the working electrodes.

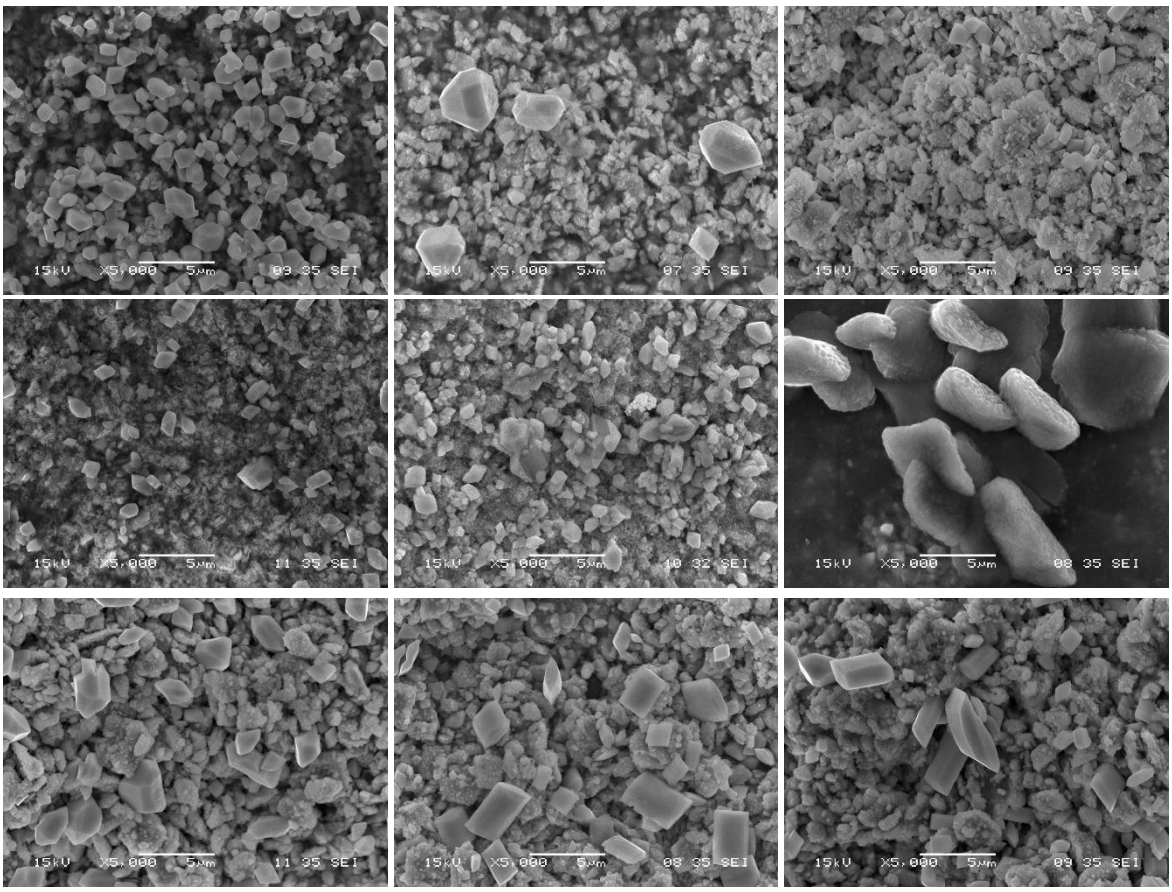

Fig. 4.11 – Comparisons 60, 300, & 600 Cycles, LO (Top), LOBS (Center), & Mix54 (Bottom)

Graphical representations of the average $PbSO_4$ crystal size (length), as a function of cycle count for the LO, LOBS, & Mix 54 samples is shown in Figure 4.12. The modest increases in the percentage change in average crystal size relative to the initial average crystal size likely indicate that the number of cycles endured or the cycling parameters were not sufficient conditions for sulfation. Additionally, the challenges encountered during the testing may have also contributed to the unexpected results.

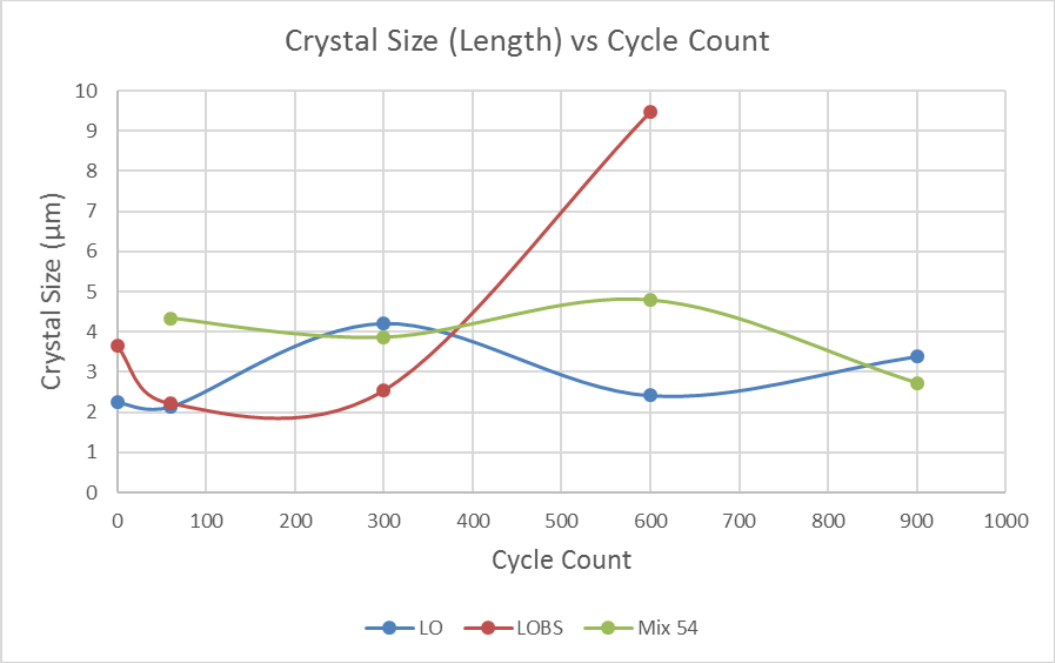

Fig. 4.12 – Crystal Size (Major Diameter) vs Cycle Count

Analysis of the average crystal size (area) after the samples were subjected to 60, 300, and 600 cycles, revealed similar trends to the average crystal size (length) evaluation. A similar initial increase in the average crystal areas for the LO and LOBS samples was observed, along with a slight decrease in the average crystal area for the Mix 54 sample from the 60 – 300 cycles, as shown in Table 4.9. Following the initial increase observed with the

LO and LOBS samples, the LO sample was observed to decrease in average crystal area between 300 and 600 cycle samples. The LOBS sample was found to have a significant increase in average crystal area between the 300 – 600 cycles. After the initial decrease in average crystal area observed for the Mix 54 sample from the 60 – 300 cycles, an increase in average crystal area occurred between 300 – 600 cycles.

Table. 4.9 – Average Crystal Size (Area) Table for 60, 300, & 600 Cycles

Sample Designation	Average Crystal (Area), μm²		
	60 Cycles	300 Cycles	600 Cycles
LO	1.88	7.30	2.40
LOBS	1.94	1.98	23.10
Mix 54	6.49	4.85	6.04

Analysis of the percent changes in average crystal size (area) after the samples were subjected to 60, 300, and 600 cycles, revealed a substantial increase for the LO sample, with roughly 288% change relative to the initial average crystal area. The LOBS and Mix 54 samples revealed more moderate changes in average crystal area of roughly a 2% increase and 25% decrease, respectively, as shown in Table 4.10. The changes in the average crystal area for the LOBS varied less than the crystal size (length), whereas the LO and Mix 54 exhibited greater variances in area when compared to the observed changes in crystal size (length). Following the initial substantial increase observed with the LO sample, the LO sample was observed to decrease roughly 67% in average crystal area between 300 and 600 cycle samples. The LO sample increased roughly 28% in average crystal area after 600 cycles relative to the initial crystal area. The LOBS sample exhibited a dramatic percent change in average crystal area between 300 – 600 cycles, growing roughly 1,067%, culminating in a total percent change of nearly 1,091% relative to the initial average crystal area. After the

initial decrease in average crystal area observed for the Mix 54 sample from the 60 – 300 cycles, a moderate increase in average crystal area occurred between 300 – 600 cycles. The Mix 54 exhibited moderate percent changes in average crystal area throughout the cycling duration, decreasing roughly 7% relative to the initial average crystal area, which suggests the observed increases in average crystal size (length) were counteracted by decreases in average crystal size (width).

Table. 4.10 – Intercycle Percent Change in Average Crystal Size (Area) Table

Sample Designation	% Change in Average Crystal (Area), μm²		
	60 – 300 Cycles	300 – 600 Cycles	60 – 600 Cycles
LO	288.30	-67.12	27.66
LOBS	2.06	1,066.67	1,090.72
Mix 54	-25.27	24.54	-6.93

Graphical representations of the average $PbSO_4$ crystal size (area), as a function of cycle count for the LO, LOBS, & Mix 54 samples is shown in Figure 4.13. The observed variances in the percentage changes in average crystal area relative to the initial average crystal areas, similar to the observations concerning the average crystal length, indicate that the number of cycles endured or the cycling parameters were not sufficient conditions for sulfation. Again, the challenges encountered during the testing may have also contributed to the unexpected results.

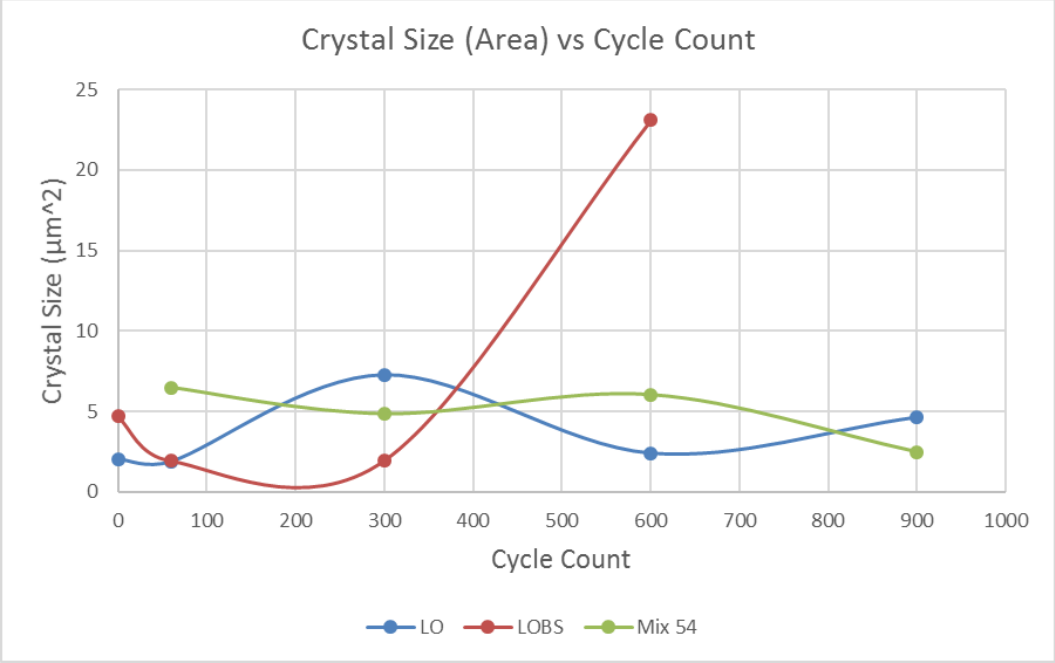

Fig. 4.13 – Crystal Size (Area) vs Cycle Count

4.1.3 Dynamic Charge Acceptance as a Function of Cycling

Dynamic Charge Acceptance (DCA) as a function of cycling was calculated from CV curves at 5, 12, 24, 36, 48, and 60 cycles for the LO, LOBS, Mix 54, CNT CMC-2, and CNT LS-2 samples. The CV curves from the first 60 cycles represented the highest cycle count with high fidelity CV curves. Challenges encountered while carrying out the experiments, precluded DCA calculation at higher cycle counts, as well as for some of the cycles analyzed.

A graphical representation of the average DCA at the aforementioned cycle counts for the analyzed samples are shown in Figure 4.14. With the exception of the Mix 54 sample, the other samples containing additives were found to exhibit the highest initial DCA. Mix 54 had both the barium sulfate, as well as two different types of carbon additives, whereas the other samples containing additives (LOBS, CNT CMC-2, & CNT LS-2) contained only one additive per their respective samples. The combination of the additives may have been responsible for the lower initial DCA.

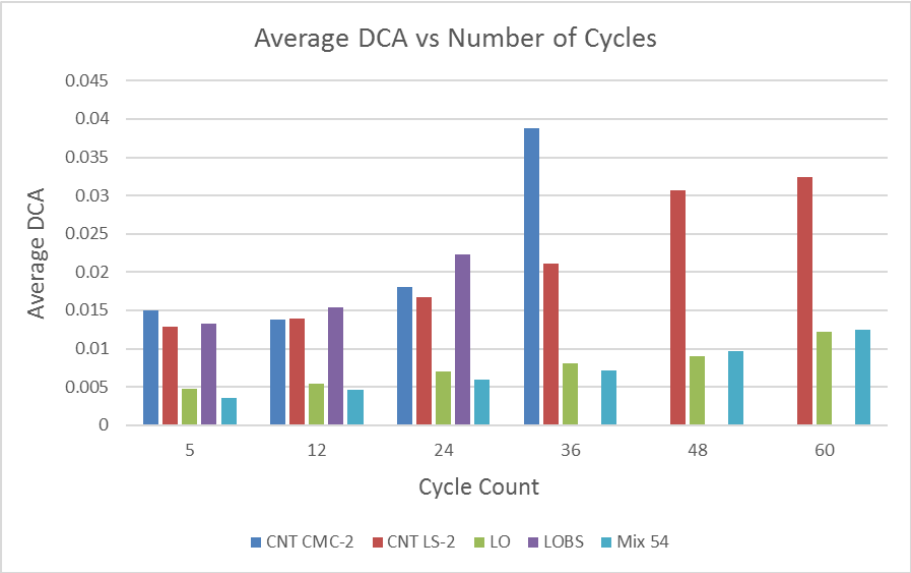

Fig. 4.14 – Average DCA vs Cycle Count

Analysis of the percent changes in average DCA relative to the initial average DCA at 5 cycles, for each of the analyzed samples is shown in Table. 4.11. All samples, with the exception of the CNT CMC-2 sample, had positive increases in their percent change in average DCA from 5 to 12 cycles. At every cycle count evaluated thereafter, all samples were found to have positive increases in their percent change in average DCA relative to the initial average DCA, which was evaluated at 5 cycles.

Table. 4.11 – Percent Change in Average DCA vs Initial Average DCA

Sample Designation	% Change in Average DCA vs Initial Average DCA				
	12 Cycles	24 Cycles	36 Cycles	48 Cycles	60 Cycles
LO	13.01	47.85	68.58	89.49	154.77
LOBS	15.38	67.14	-	-	-
Mix 54	33.46	70.59	103.07	176.59	256.22
CNT CMC-2	-7.84	20.45	159.23	-	-
CNT LS-2	7.99	30.56	64.69	138.26	152.20

A graphical representation of the percent change in average DCA relative to the initial average DCA at 5 cycles, for each of the analyzed samples is shown in Figure 4.15. Mix 54 was observed to have the largest percent change relative to the initial DCA for every cycle count evaluated, with the exception of the CNT CMC-2 sample after 36 cycles. The continued increase in DCA from 5 – 60 cycles suggests potentially that the samples did not undergo a sufficient formation process. It is also possible that the cycle duration was not sufficient for sulfation to occur, which would have been observed as a decrease in DCA.

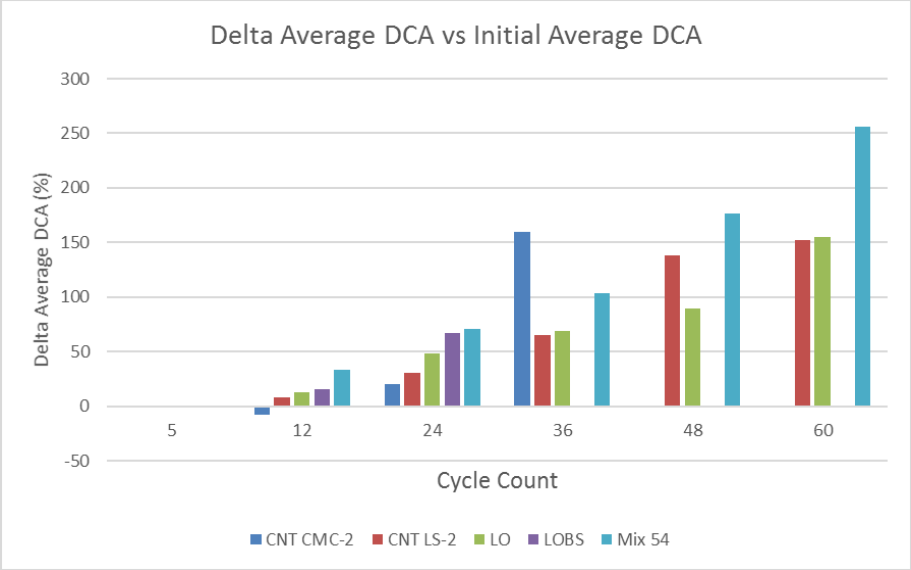

Fig. 4.15 – Delta Average DCA vs Initial Average DCA

Analysis of the percent changes in average DCA relative to the previous cycles average DCA for each of the analyzed samples is shown in Table. 4.12. The percent change in average DCA between the 12 and 24 cycles revealed similar changes in average DCA amongst all samples. The percent change in average DCA did not exceed 50% between cycles with the exception of the 24 – 36 cycle for the CNT CMC-2 sample, which was the largest inter-cycle percent change in average DCA.

Table. 4.12 – Percent Change in Average DCA vs Previous Cycle Average DCA

Sample Designation	% Change in Average DCA vs Previous Cycle Average DCA				
	5 – 12 Cycles	12 – 24 Cycles	24 – 36 Cycles	36 – 48 Cycles	48 – 60 Cycles
LO	13.01	30.83	14.02	12.40	34.45
LOBS	15.38	44.86	-	-	-
Mix 54	33.46	27.82	19.04	36.20	28.79
CNT CMC-2	-7.84	30.70	115.21	-	-
CNT LS-2	7.99	20.90	26.13	44.67	5.85

A graphical representation of the percent changes in average DCA relative to the previous cycles average DCA, for each of the analyzed samples is shown in Figure 4.16. The inter-cycling percent change in average DCA overall revealed increases and decreases in average DCA, as opposed to a theoretically expected decline in DCA with cycling. This observation suggests the samples likely did not exhibit sulfation within the cycle period evaluated.

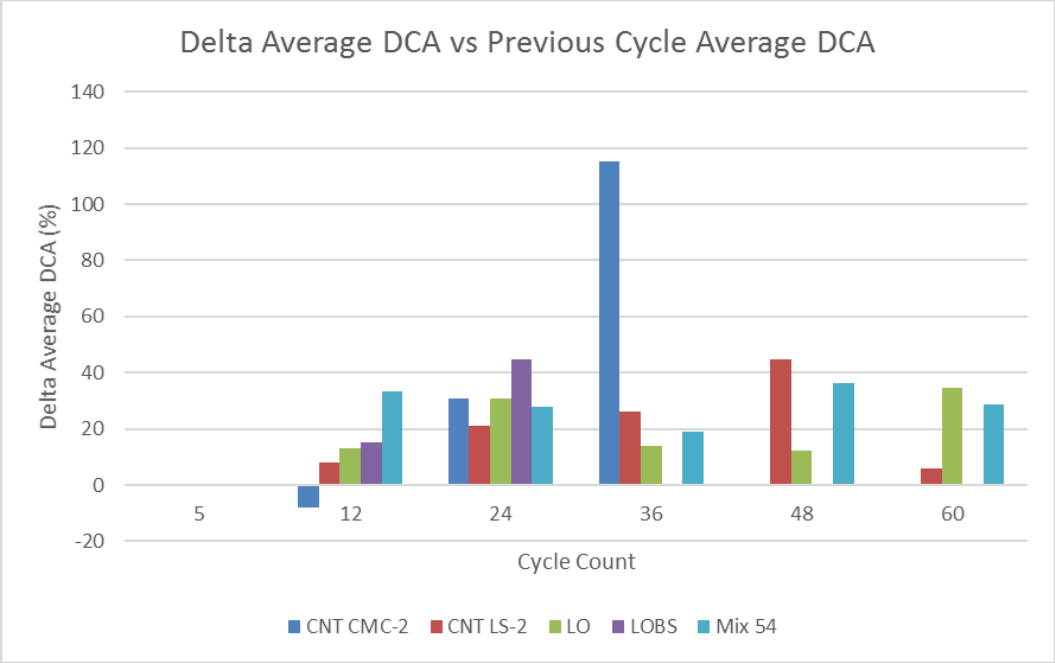

Fig. 4.16 – Delta Average DCA vs Previous Cycle Average DCA

4.2 Impacts of NAM Additives

The different NAM additives were responsible for significant differences relative to the LO control sample. The addition of barium sulfate to the NAM slowed the growth rate roughly 80% while looking at crystal size (length), and roughly 368% while looking at crystal size (area), when compared to the control between 1 – 36 hour coarsening times.

The addition of the VAN G and PBX 135A additives present within the Mix 54 sample, in addition to the barium sulfate, resulted in a 52% reduction crystal size (length) growth, and 42% reduction in crystal size (area) growth, when compared to the control between 1 – 36 hour coarsening times.

The addition of the CNT additives to the NAM resulted in an initial crystal size (length) roughly 45% (CNT CMC-2) and 39% (CNT LS-2) of the initial crystal size (length) of the LO control sample. The observed average crystal size (length) of both the CNT CMC-2 and CNT LS-2 samples were found to be roughly 93% and 45% the size of the average crystal size (length) of the LO control sample at 36 hours at 96 hours, which represents a significant retardation in crystal growth. Observations of the crystal size (area) comparisons were found to exhibit similar trends.

All NAM additives were found to contribute to a higher initial average DCA, as well as larger percentage increases in average DCA relative to the initial average DCA with increases in cycle counts, relative to the LO control sample.

The presence of additives to the NAM relative to the LO control sample, as it pertains to crystal size (length), crystal size (area), and DCA, were found to have significant impacts to NAM performance.

4.3 Impacts of the Form of Carbon Additives

The VAN G carbon additive present within the Mix 54 sample was a carbon additive with a high surface area. The CNT CMC-2 and CNT LS-2 carbon additives were carbon nanotubes, and thus have vastly different material properties when compared to the Mix 54 carbon additive, which became evident throughout the experiments conducted.

The CNT samples both had roughly a third smaller average crystal size (length) after 1 hour of coarsening relative to the Mix 54 sample. This trend was found to continue, when the CNT samples both had smaller average crystal sizes after 12 hours of coarsening, than the Mix 54 sample after 36 hours of coarsening.

When looking at the average DCA with respect to cycle count, the CNT samples were found to have up to 5 times higher initial DCA compared with to the Mix 54 sample. Even after 60 cycles, the CNT LS-2 sample still had roughly 2.5 times the DCA of the Mix 54 sample.

The form of the carbon additives as it pertains to crystal size (length), crystal size (area), and DCA, were found to have significant differences, that manifested in better NAM performance.

4.4 Comparisons

4.4.1 Comparisons of Crystal Growth Coarsening Times

This analysis found an increase in both crystal size and crystallinity with an increase in time. All cells were cycled for 60 cycles and then left to coarsen for various periods of time. A gradual increase in crystal length was found to be evident up to the 36 hour mark, as evident in Figure. It should be noted that at 96 hours crystal size diminished. The cause for the decrease in crystal size is not known. This trend was evident for all of the samples analyzed.

4.4.2 Comparisons of Crystal Growth Different Cycles

This analysis revealed no significant correlation with regards to differences in crystal growth for the differences in cycles from 60 cycles to 900 cycles, for any of the samples analyzed. This observation likely indicates that the number of cycles endured and/or the cycling parameters used were not sufficient conditions for sulfation to have occurred.

4.4.3 Comparisons of Dynamic Charge Acceptance with Cycling

This analysis found DCA increased from the initial average DCA values for all samples evaluated with respect to increases in cycling. This observation suggests potentially that the samples did not undergo a sufficient formation process. It is also possible that the cycle duration was not sufficient for sulfation to occur, which would have been observed as a decrease in DCA with an increasing in cycling. Additionally, the challenges that were encountered during the experiment, specifically with regards to delamination of the NAM on the working electrode, as well as corrosion of the current collectors, likely contributed to the less than ideal resultant CV curves above 60 cycles.

4.5 Challenges

4.5.1 Corrosion of Current Collectors

Corrosion of the monel alloy used as the current collectors for the three-electrode setup was found to be evident. The corrosion event was limited to the side with the platinum counter electrode. It is suspected that a galvanic interaction occurred between the platinum counter electrode and the monel alloy current collector. In order to mitigate the corrosion of the current collectors, a different material should be utilized. The ideal material would have a high electrical conductivity and should not corrode in the electrochemical environment. Utilizing lead rods would be ideal so as not to affect the electrochemistry of the cell. If the lead rods would not work, a Teflon rod similar to the one used to stabilize the reference electrode could be utilized in conjunction with a thin platinum wire through the center as a current conductor.

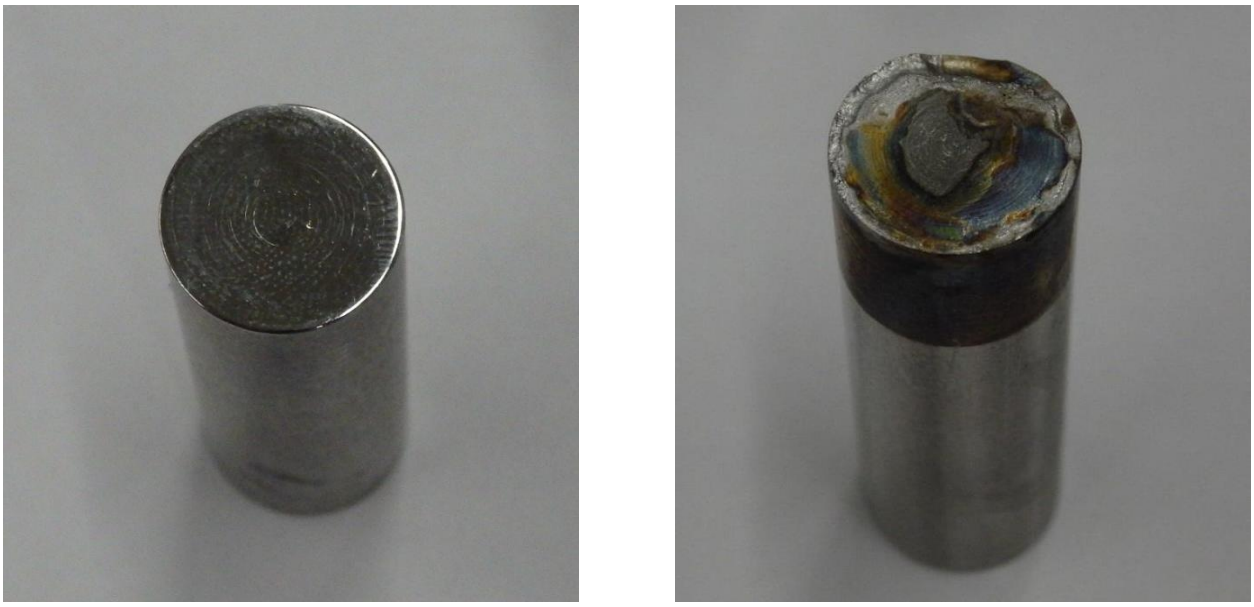

Fig. 4.17 –Current Collector Initial Condition (Left), Current Collector after 900 Cycles (Right)

4.5.2 Delamination of the Working Electrode

The NAM paste was found to have a loss of adhesion occurring during high cycle numbers. It was suspected that the lack of adhesion was attributed to a lack of abrasion to the lead foil. Also, at high cycles the lead foil began to degrade. This could also contribute to a lack of fully transformed material. It is unclear as to when the delamination of the NAM material occurred, and the delamination was not consistent. The samples were abraded with the use of a Scotch Brite pad. Possible mitigation strategies in order to avoid the delamination of the NAM would be to utilize a different binder other than PVDF. Other than utilizing a different binder, possibly a different thickness in lead foil could be utilized.

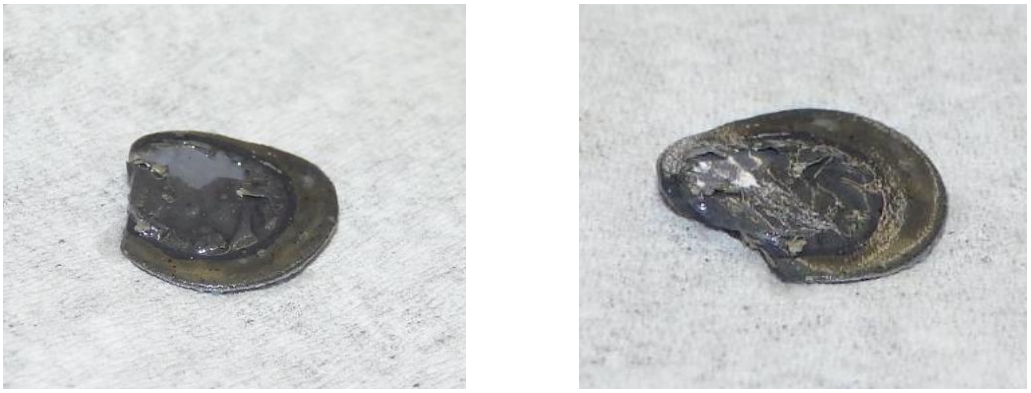

Fig. 4.18 –Representative Images of Delamination of Working Electrodes

4.5.3 Lack of Homogenous NAM Additive Distribution

The barium sulfate additive present within both the LOBS sample and Mix 54 sample, along with the carbon and lignin additive, VAN G and PBX 135, that were added to the Mix 54 sample, were mixed with the leady oxide prior to the addition of the PVDF and NMP, for the preparation of the aforementioned samples. During the pasting procedure, gradients in the distribution of the additives were observed, as shown in Figure 4.19.

Fig. 4.19 – Representative image of non-homogenous NAM additive distribution

The non-homogenous distribution of the additives likely affected the electrochemical performance amongst the individual cells of their respective samples. The CNT additives, in comparison, were suspended in solution, which may have contributed to a more homogenous distribution of the additives within the NAM paste. Possible mitigation strategies for the observed non-homogenous distribution of the additives would be to mix the components of the NAM paste in smaller batches, subsequently combining them. With smaller batches of the components mixed together, it might allow for better mixing. Additionally, various frequency settings or mixing time could be used on the acoustic mixer, in order to better mix the samples.

4.5.4 Outgassing

The specific voltage ranges used during the testing of the samples led to potential ranges where both hydrogen and oxygen evolution potentials were realized. Vented grooves were added to the Teflon support for the reference electrode holder to allow for pressure release. Additionally, the test set up was tilted slightly to allow gas to escape via the vent. During early portions of the testing an upright setup was utilized. This upright setup allowed for the evolved hydrogen to enter the reference electrode in the form of bubbles. The presence of bubbles within the reference electrode became problematic when the gas bubble blocked electrical contact with the electrolyte solution resulting in a voltage range outside of the parameters allowed by the Arbin battery tester. The voltage ranges could be altered slightly to minimize the evolution of both hydrogen and oxygen.

Chapter 5 – Summary

As the auto industry constantly evolves to meet the ever-increasing demands of the consumer, the implementation of sustainable, safe, and economically feasible methods of both storing and supplying the large concentrations of energy required to drive the new technologies will without a doubt be required. The energy storage technology reported in this work sheds light on an early solution to this prescient crisis, via further optimization of a mature technology.

As the advancement of lead acid battery construction has improved over the years, there has been an increased interest in the utilization of the lead acid battery chemistry for usage in HEVs. However, new technologies employed in HEVs for energy conservation such as start-stop and regenerative braking, imparts new demands on the legacy technology. As such, methods for the evaluation of NAM additives efficacy in the retardation of lead sulfate crystallization and growth kinetics, along with dynamic charge acceptance of the negative plates are necessitated. CV analysis has become an essential analytical technique for rapid evaluation of NAM additives for the electrochemical properties. The work provided here has proven the method's competency in analyzing the complexities of the kinetics of lead sulfate crystal nucleation and growth, along with changes in dynamic charge acceptance, in a more timely and efficient manner when compared to traditional means.

In this study, cyclic voltammetry techniques were employed to cycle the test cells between oxidation and reduction potentials. The aforementioned testing aided in

determining how variations in the number of cycles endured, coarsening duration, and NAM additives impacted the DCA, as well as influence the growth kinetics of lead sulfate crystals. From the results it was concluded that the coarsening duration had the largest influence on crystal growth. It was further determined that the carbon additives had the largest impacts in the retardation of lead sulfate growth kinetics, as well as exhibiting some of the highest observed DCA values of the samples analyzed. The following address the limitations, findings, and future research directions of the current thesis.

5.1 Limitations

- The testing method developed to study the lead sulfate reduction kinetics on the negative plate were evaluated on a half-cell as opposed to a full cell.
- The HEV cycling parameters employed during testing may not be representative of the C-rates observed during real world applications.
- The binders used for the fabricated working electrodes may differ from binders used in industry.

5.2 Findings

Cyclic Voltammetry was used to cycle a three-electrode test cell with simulated HEV parameters. The working electrodes for the test cell, consisted of five NAM paste recipes containing different additives, which were subsequently adhered to abraded lead foil. The working electrodes opposed a platinum counter electrode, immersed in a sulfuric acid solution. Scanning Electron Microscopy, was used to conduct dimensional analysis of the lead crystals that precipitated onto the NAM during testing, along with the resultant CV curves, which were used to calculate DCA for the test samples, from which the following findings were observed:

- The presence of additives within the NAM matched theoretical predictions with respect to the promotion of crystal nucleation over crystal growth, resulting in observed smaller average crystal size, as well as exhibiting less faceting, suggesting a more amorphous crystal, which is more readily able to dissolve, relative to the leady oxide only control sample.
- The observed lead sulfate growth rate for the CNT samples subjected to varying coarsening times, were found to meet theoretical predictions of following a parabolic growth rate, by exhibiting near perfect linearity when plotting average crystal size vs square-root of coarsening time.
- Varying the number of cycles, the cell experienced, did not yield statistically meaningful differences in average crystal size or growth kinetics.
- Average DCA values were found to have increased from the initial average DCA values for all samples evaluated with respect to increases in cycling.
- CNTs additives induced the most significant effects among all trials, resulting in greater than 40% smaller average initial crystal size relative to the control sample. With respect to initial average DCA, the CNT samples were found to have up to 5 times higher initial DCA.
- Corrosion of the current collectors during cycling is of valid concern. Securing the working electrode to the current collectors with teflon tape was found to minimize the amount of corrosion of the current collectors by serving as a seal.
- Insufficient abrasion of the lead foil was the suspected root cause for the observed localized lack of adhesion of the NAM paste.

- Non-homogenous distribution of NAM additives was observed to have occurred, which likely affected the electrochemical performance of the individual cells within the same sample set.

5.3 Future Works

5.3.1 Additional Cycling time

Analysis of the differences in crystal size did not change significantly from 60 cycles to the maximum tested at 900 cycles. The longest cycle time was determined by what was realistically feasible on a time scale to complete testing in an appreciable time frame. It would be interesting to run some longer duration time scales to see if the growth kinetics are affected. If possible, the cycling parameters should reflect HEV cycling, specifically focusing on HRPSoC conditions.

5.3.2 Full Cell Analysis

This analysis utilized a three-electrode setup of a half cell. The primary focus was on the negative terminal due to its applicability in industry for hybrid vehicles and their use of regenerative braking technologies and start-stop technologies, which impart high current and operation of the battery at partial state of charge, which results in increased battery degradation. Running testing on a full cell would allow for analysis of the positive terminal in conjunction with the negative terminal and analyze its affects with regards to growth kinetics. It is suspected that the competing reactions occurring at the two electrodes could contribute to differences in lead sulfate crystallization.

5.3.3 Temperature Dependence

The typical operating temperature of a SLI battery is -40 – 70 °C, which an appreciable range relative to the room temperature testing that was conducted. Theoretically, elevated temperature should cause an increase in the growth kinetics of the lead sulfate crystals due to higher electrochemical activity, and by extension, cooler temperatures should serve to slow the electrochemical activity. The degree to which this affects the growth kinetics of lead sulfate were not studied in this work.

5.3.4 Difference Electrolyte Solution

The specific gravity of 1.28 g/mL was chosen to closely resemble what is used in industry for applicability of the research findings. In order to develop a deeper understanding of the underlying mechanism of the growth kinetics of the lead sulfate crystals. It is suspected that the amount of active species will allow for differences in mass transfer rates ultimately effecting the growth kinetics.

5.3.5 Carbon Morphological Effects

Various forms of carbon additives to the NAM were evaluated for their effects on the lead sulfate growth kinetics. The carbon nanotube additives were found to have the greatest impact on the retardation of crystal growth. The developed testing method could be used to explore carbon nanotubes that exhibit different chirality, diameters, or lengths, to evaluate their contributions to the observed slowing of the lead sulfate crystal growth kinetics.